Available online at www.sciencedirect.com

ScienceDirect

Geochimica et Cosmochimica Acta 276 (2020) 299–326

Geochimica et Cosmochimica Acta

www.elsevier.com/locate/gca

Volatiles in lunar felsite clasts: Impact-related delivery of hydrous material to an ancient dry lunar crust

J.I. Simon [a,*], R. Christoffersen [a,b], J. Wang [c], M.D. Mouser [a,1], R.D. Mills [d], D.K. Ross [a,b,e], Z. Rahman [b], C.M.O'D. Alexander [c]

[a] *Center for Isotope Cosmochemistry and Geochronology, Astromaterials Research and Exploration Science, NASA Johnson Space Center, Houston, TX 77058, USA*

[b] *Jacobs, NASA Johnson Space Center, Mail Code XI3, Houston, TX 77058, USA*

[c] *Department of Terrestrial Magnetism, Carnegie Institution of Washington, Washington, DC 20015-1305, USA*

[d] *Department of Geological Sciences, University of North Carolina, Chapel Hill, NC 27599, USA*

[e] *University of Texas at El Paso/Jacobs-JETS, Houston, TX 77058, USA*

Received 16 April 2019; accepted in revised form 12 February 2020; available online 26 February 2020

Abstract

In this detailed geochemical, petrological, and microstructural study of felsite clast materials contained in Apollo breccia samples 12013, 14321, and 15405, little evidence was found for relatively enriched reservoirs of endogenic lunar volatiles. NanoSIMS measurements have revealed very low volatile abundances (≤2–18 ppm hydrogen) in nominally anhydrous minerals (NAMS) plagioclase, potassic alkali feldspar, and SiO_2 that make up a majority of these felsic lithologies. Yet these mineral assemblages and clast geochemistries on Earth would normally yield relatively high volatiles contents in their NAMS (~20 to ≥80 ppm hydrogen). This difference is particularly notable in felsite 14321,1062 that exhibits extremely low volatile abundances (≤2 ppm hydrogen) and a relatively low amount of microstructural evidence for shock metamorphism given that it is a clast of the most evolved (~74 wt.% SiO_2) rock-type returned from the Moon. If taken at face value, 'wet' felsic magmas (~1.2–1.7 wt.% water) are implied by the relatively high hydrogen contents of feldspar in felsite clasts in Apollo samples 12013 and 15405, but these results are likely misleading. These felsic clasts have microstructural features indicative of significantly higher shock stress than 14321,1062. These crustal lithologies likely obtained no more water from the lunar interior than the magma body producing 14321,1062. Rather, we suggest hydrogen was enriched in samples 12013 and 15405 by impact induced exchange, and/or partial assimilation of volatiles added to the surface of the Moon by a hydrated impactor (asteroid or comet) or the solar wind. Thus, the best estimate for magmatic water contents of felsic lunar magmas comes from 14321,1062 that leads to a calculated magmatic water content of ≤0.2 wt.%. This dry felsic magma has a slightly greater, but comparable water content to the ancient mafic magmas implied by the other lithologies that we have studied. Based on this and expanding evidence for a significantly dry ancient or early degassed Moon it is likely that some recent estimates (100's ppm) of the water abundances in the lunar parental magma ocean have been overestimated.

Keywords: Lunar; Volatiles; Felsic clasts; Microstructures; Shock features

1. INTRODUCTION

The long-standing anhydrous view of the Moon's interior has been challenged recently by a growing number of sample and remote sensing studies (Saal et al., 2008;

* Corresponding author.
E-mail address: Justin.I.Simon@NASA.gov (J.I. Simon).
[1] Current address: Department of Earth and Planetary Sciences, The University of Tennessee, Knoxville, TN 37996, USA.

https://doi.org/10.1016/j.gca.2020.02.008
0016-7037/Published by Elsevier Ltd.

McCubbin et al., 2010; Boyce et al., 2010; Hauri et al., 2011; Greenwood et al., 2011; Jolliff et al., 2011; Bhattacharya et al., 2013; Hui et al., 2013; Klima et al., 2013; Barnes et al., 2014; Tartese et al., 2014; Milliken and Li, 2017; Mills et al., 2017; Petro et al., 2013). Understanding the volatile budget of the Moon is important for understanding the distribution of volatiles in the Solar System, how their distribution changed as the Solar System evolved, and because volatiles control the physiochemical properties of magmas, including degassing, which can have significant effects for both local and planetary scale differentiation (Albarede, 2009). Although the interior of the Moon can no longer be considered anhydrous, the lack of hydrous mineral phases in Apollo samples and the reduced mineralogies of many lunar rocks, complicate recent estimates for high magmatic water contents (Mills et al., 2017), and moderate to Earth-like amounts of hydrogen for the bulk Moon (Hauri et al., 2011, 2015; Hui et al., 2013, 2017). Given that nearly all petrogenetic processes enrich incompatible elements and molecular species (including water) during formation of chemically differentiated melts on Earth (i.e., felsic melts), investigating the abundances of volatiles in lunar felsic rocks provides an obvious point of reference to test the possibility of Earth-like volatile abundances in the Moon's interior.

Silicic volcanic features on the surface of the Moon exhibit a range of landforms and are generally found within the Porcellarum KREEP Terrane (PKT), the exception is the Compton-Belkovich complex (CBC) (Jolliff et al., 2011). Greater recognition of their size, abundance, and wide distribution by recent remote sensing studies (Jolliff et al., 2000; Hagerty et al., 2006; Glotch et al., 2010), has generated renewed interest in the role that silicic magmatism has played in the evolution of the Moon. Understanding the formation processes of felsic rocks will contribute significantly to our expanding knowledge of "major" lunar magma types. Furthermore, because felsic magmas ought to concentrate volatiles during their formation and carry them to the surface, never to be recycled back into the interior, their generation potentially represents a critical global volatile differentiation process as well as *in situ* resource for future missions. "Evolved" (i.e., silica-rich with high Th content) volcanic features identified in lunar remote sensing data sets indicate the existence of moderately large and widespread silicic centers, akin to those found in Earth's continental crust. However, silicic clasts contained in complex impact breccias and found in regolith are rare and typically small in samples from Apollo sites (Ryder, 1976; Warner et al., 1978; Quick et al., 1981; Warren et al., 1983; Marvin et al., 1991; Ryder and Martinez, 1991).

Glasses and clasts of evolved silicic material (~68–80 wt. % SiO_2 and ~4–7 wt.% K_2O) are present in minor amounts in a number of Apollo samples and some lunar meteorites (Roedder and Weiblen, 1970; Stoeser et al., 1974; Ryder et al., 1975; Ryder, 1976, Warner et al., 1978; Quick et al., 1981; Warren et al., 1983; Seddio et al., 2013). In this study, we focus on fragmental crystalline rock clasts as opposed to material contained in the mesostasis of lunar basalt. The latter may represent evidence of local silicate liquid immiscibility or SLI (Rutherford et al., 1976), whereas the fragments are more likely to be samples of volumetrically significant evolved rock units. Various possible origins for such units, including fractional crystallization/-partial melting of more mafic precursor magmas/rocks have been proposed (Seddio et al., 2013), but no models for their formation are widely accepted as of yet.

The modal compositions of the felsic rocks investigated in this study are dominated by potassic alkali feldspar and a silica phase (either quartz or a higher temperature polymorph). Variable modal amounts of intermediate plagioclase also occur, however, across our sample assemblages. The alkali feldspar itself also can contain enough albite and anorthite component to make it deviate substantially away from nominal end-member K-feldspar. Because all of these compositional variations along with the associated sample microstructures have the potential to provide important petrogenetic clues to correlate with measured volatile abundances, we have documented these through detailed coordinated analyses using a range of techniques and at a range of imaging and analytical scales.

Although they are nominally anhydrous minerals (NAMS), the feldspars, including alkali feldspar, and the silica polymorphs are known from terrestrial igneous rocks to contain trace structurally bound hydrogen-related defects, dominantly in the form of OH^- and/or H_2O (Johnson, 2006). Terrestrial feldspars in particular can contain up to 1500 ppm "water", that is typically speciated as OH^- and/or molecular H_2O, with variations across the feldspar group with regard to the detailed spectroscopic signature of the accommodating H-related defect (Kronenberg, et al., 1996; Johnson and Rossman, 2003, 2004; Mosenfelder et al., 2015).

For feldspars in lunar rocks, the initial focus has been on trace water contents in plagioclase making up the earliest, least evolved, crustal rocks from the lunar magma ocean (Hui et al., 2013, 2017). This work first explored the feasibility of using feldspar, together with relevant H partition coefficients, to measure the water and other volatile contents of lunar magmas. Here we have made use of feldspar, and to a lesser extent quartz, as probes for water contents in rocks at the other end of the lunar petrogenetic spectrum expanding our initial first-of-its-kind work (Mills et al., 2017). As previously noted, among the diverse elements of importance of these rocks to lunar petrogenesis is their possible use as upper limit indicators for overall volatile content of the Moon. In line with this our initial hypotheses were that felsic rocks would contain some of the highest water contents among lunar materials and that any that did not would have strong physical evidence for disturbance, i.e., impact processing. It turns out that neither of these expectations were substantiated, in fact the opposite was observed. In order to address the petrogenesis and shock history of the studied clasts, coordinated microstructural investigations of the host minerals of each volatile measurement were conducted, and expanded mineralogical and textural studies of related materials have been undertaken. We present volatile abundances measured in a variety of ancient lunar materials and generally find evidence for only nominal amounts of water in most of the studied materials including some felsic materials. Notable exceptions are found in some felsic materials that

have textures that indicate complex impact histories, implying that this "abundant" water is potentially exogenous to the early Moon. It would therefore seem that exogeneous water was locally added to the Moon through impacts from the time before complete crystallization of the lunar magma ocean (Greenwood et al., 2011; Svetsov and Shuvalov, 2015; Barnes et al., 2016a; Daly and Schultz, 2018), until at least the formation of the early lunar crust (~4.3 Ga) (Tartèse and Anand, 2013; this work), and possibly even more recently (Joy et al., 2012; Kayama et al., 2018).

2. SAMPLES

This study utilized NanoSIMS methods to measure H and other trace volatile contents predominantly in feldspars in mm-size rock chips from Apollo lunar breccias 12013, 14303, and 15405, and in feldspar and SiO_2-quartz mineral separates from breccia 14321. The specific allocation numbers, relevant parent material, and curatorial processing information for the measured samples are listed in Table 1. The parent breccias are known hosts for complexly distributed assemblages with either granite or granite-affinity mineralogies (all here referred to as felsite). The samples used are all derived from these assemblages. Apollo sample 12013 is a complex mixture of two polymict breccias (both clast-rich with crystalline matrices) in which the felsic material occurs both as distinct clasts in regions of "black" breccia, and as more complexly distributed patchy regions in a "gray" breccia that also contains other, less-evolved, clast types (Quick et al., 1981). The gray breccia material dominated the rock chips utilized here. Most of the gray breccia felsite has a fine-grained granophyric (here referred to as microgranophyric) microstructure in which branching networks of the SiO_2 phase are intimately intergrown with feldspar in semi-skeletal, trellis-like arrangements (Quick et al., 1981). Volatile abundances were determined in feldspars within the microgranophyre, as well as in other felsic intergrowths described below that are associated with the microgranophyre patches.

Apollo sample 14321 is a fragmental crystalline matrix breccia with a diversity of lithic and microbreccia clasts that include felsite (Simonds et al., 1977; Meyer, 2016). Our trace volatile analyses were performed on feldspar and SiO_2 (quartz) mineral separates originally prepared by Shih et al. (1985) from rock chip allocation 14321,1062 derived from the granite clast 14321,1027 studied by Warren et al. (1983) (Table 1). Supporting analytical field-emission scanning electron microscope (FE-SEM) and electron-probe microanalysis (EPMA) work was also performed using 14321 thin sections 1493, 1494, and 993 that contain fragments of the 14321,1027 granitic clast (Table 1). Although described by Warren et al. (1983) as having a granophyric microstructure broadly similar to that of the 12013 gray breccia felsite, the 14321,1027 intergrowth has a coarser (100–150 μm), more uniform grain size. It is also modally less diverse, being a true K-feldspar granite consisting of nearly 98% SiO_2 (quartz) and K-rich alkali feldspar, with no second feldspar and only traces of ferromagnesian phases. The crystalline feldspar-quartz assemblage is converted to shock-melted glass in localized areas, where the granite assemblage is preserved it shows minimal other shock effects, except for widely spaced fractures.

The third felsic clast type studied here comes from the Apollo 15405 breccia (Ryder, 1976; Marvin et al., 1991; Ryder and Martinez, 1991). 15405 is described as a clast-bearing impact melt rock with an igneous-textured crystalline matrix (Meyer, 2016). Ryder (1976) described it as containing a "distinctive and limited" lithic fragment population, including coarse grained granite, KREEP-rich quartz-monzodiorite (QMD), and KREEP basalt (Ryder, 1976). Here we investigate in more detail the microgranophyre clasts in 15405,78 studied recently by Mills et al. (2017), as well as other felsic clasts from material allocated to us extracted from this breccia. Ryder (1976) showed polarized light images of crystalline alkali feldspar-SiO_2 granophyric intergrowths, in thin sections of 15405 felsite clasts, in which the SiO_2 phase is dark while alkali feldspar exhibits its expected birefringence. The large clast fragments consist mainly of plagioclase, clinopyroxene, SiO_2 phase, and alkali feldspar, with accessory ilmenite, troilite, Fe-metal, chromite, and phosphate (Ryder, 1976). The intergrowth of alkali feldspar and silica are relatively fine grained, as compared to those seen in the 14321 clast materials, and more like those in the 12013 microgranophyre.

To provide a comparison to our work on the 12013, 14321, and 15405 felsite assemblages, we also studied mafic igneous clasts from crystalline-matrix breccia 14303 (Meyer, 2016), and 15405, including examples of a troctolite (14303,363), and an alkali-rich "KREEP basalt" (15405,255). Olivine and plagioclase dominate the comparatively coarse-grained troctolite. The medium-grained KREEP basalt has an equigranular texture and a similar mineralogy (abundant plagioclase and orthopyroxene and more minor clinopyroxene and olivine) to that of QMD from 15405 (Ryder, 1976), with the exception that it lacks an obvious silica phase.

3. METHODS

3.1. Low-contamination Indium Sample Mounting

Use of conventional epoxy resin sample mounting methods for NanoSIMS analyses can result in analytical artifacts when making low abundance volatile measurements (e.g., Boctor et al., 2003). Brecciated materials are fractured and resins penetrate into these fractures that cannot be removed. Clast material extracted from lunar breccias also tends to be relatively small in terms of the typical ion microprobe sample mounts, i.e., ~1 inch or 1 cm-rounds. In order to minimize contamination of the sample materials as well as volatile background related to sample mount outgassing, we employed a sample preparation method using indium metal instead of organic resin (Hauri et al., 2002; Koga et al., 2003; Usui et al., 2012, 2015). The method uses sample mounts prepared by first pressing heat-softened indium metal into round openings a few mm in diameter that were drilled into the center of 1 inch or 1 cm-diameter aluminum holders. The surface of the indium is then gently flattened with a hydraulic press using a clean

Table 1
Parent materials, processing history and specific numbers of samples used for trace volatile measurements and supporting characterizations.

Parent Apollo rock sample number	Specific number of allocated sample used in current study	Description	Sample principal lithology	Parent samples, description, sample number(s)	References
12013	**12013,141**	mm to sub-mm rock fragments hand-selected from allocated *chip fragment group* **12013,141**	*Microgranophyric felsite with other felsite assemblages*	*Chip fragment group* **12013,141** from disaggregated piece of "gray breccia" derived from rock slab fragments **12013,8**	Quick et al. (1981), petrology; Shih et al. (1993), geochronology; Meyer (2016), curatorial
	12013,167	0.4–0.5 mm gray breccia rock fragments hand-selected from allocated *chip fragment group* **12013,156**	*Microgranophyric felsite with other felsite assemblages*	*Chip fragment group* **12013,156** produced as by-product of wire saw processing that made whole rock slab **12013,11** (displays abundant gray breccia on cut face)	
14303	**14303,363**	mm to sub-mm rock fragments hand-selected from allocated *chip fragment group* **14303,363**	*Troctolite*	*Chip fragment group* **14303,363** removed from butt-end piece **14303,288** by chip processing	Warren et al. (1983), petrology; Shih et al. (1993), geochronology; Meyer (2016), curatorial
14321	**14321,1062**	149–44 μm grain size separate processed by Shih et al. (1985) from 150 mg allocation designated *chip fragment group* **14321,1062**	*Microgranophyric felsite*	*Chip fragment group* **14321,1062** sub-selected from *chip fragment group* **14321,1061** removed from lunar clast **14321,1027** visible on W_1 face of whole-rock slab sample **14321,46. (**Clast **14321,1027** has additional designation c4 in Meyer (2016))	Warren et al. (1983), Meyer and Yang (1988) mineralogy-petrology; Shih et al. (1985), Shih et al. (1993), Meyer et al. (1996), geochronology; Meyer (2016), curatorial
	14321,1493 **14321,1494** **14321,993**	3 thin sections, (particle mount type) made from *lunar clast* **14321,1027** processed as described above	*Microgranophyric felsite*	3 thin sections, (particle mount type) made from *lunar clast* **14321,1027** processed as described above	
15405	**15405,78**	mm- to sub-mm rock fragments hand-selected from allocated *chip fragment group* **15405,78**	*Microgranophyric felsite (as sub-mm clasts in dark melt breccia matrix)*	*Chip fragment group* **15405,78** derived from fragment **15405,64** chip-processed from parent rock fragment **15405,7**	Ryder (1976), Marvin et al. (1991), Mills et al. (2017), mineralogy-petrology; Meyer (2016), curatorial
	15405,255	mm- to sub-mm rock fragments hand-selected from pieces of allocated *rock chip* **15405,255**	*Mafic/basaltic rock assemblage*	*Rock chip* **15405,255** hand-selected from fragments of light colored clast **15405,93** that separated from slab piece **15405,92** during (wire) sawing	

glass microscope slide as a spacer to keep the indium surface clean. Rock chips and/or grains are then gently hand-pressed into the prepared mounts with the glass slide spacer, with the indium re-softened below the melting point by slight heating as needed. Finally, the mounts are dry-polished using a sequence of 10–1 μm alumina-in-polymer lapping films.

Allocated rock chips from the 12013, 14303, and 15405 breccias were selected for processing into indium mounts based on their presumed content of either distinct felsic clasts or distributed felsic material. For the 14321 mineral separate prepared by Shih et al. (1985), a mixture of grains from the 100–200 μm size fraction containing feldspar and silica were hand-pressed using a clean glass slide into a 1 mm-thick layer of smooth-pressed indium on a 1 cm-diameter aluminum mount, then polished using the same method as the other samples.

3.2. Analytical FE-SEM and EPMA

After receiving a carbon coat (~15 nm thick), the indium sample mounts were studied using the imaging and analytical capabilities of the JEOL 7600 FE-SEM and JEOL JXA-8530F EPMA at NASA JSC. The standard

analytical protocols employed can be found in Righter et al. (2015) and Han et al. (2020). This work was carried out to select and characterize regions before as well as after NanoSIMS analyses, and to build an on-going imaging and analytical dataset from the larger suite of mounted samples for understanding their comparative microstructures and phase compositions. In addition to the wavelength-dispersive X-ray (WDS) microanalysis capabilities of the JXA-8530F EPMA, both the SEM and EMPA are equipped for semi-quantitative analyses and compositional spectrum imaging (element mapping) using Thermo System 7 energy-dispersive (EDS) silicon drift X-ray spectrometer systems. EPMA WDS analyses of feldspars used a beam current of 15 nA and a beam diameter of 3 μm in order to reduce beam-damage and alkali element loss/volatilization. Mafic phases, such as pyroxene were analyzed with a more focused 1–2 μm beam at a beam current of 30 nA. FE-SEM imaging and EDS element mapping was performed using a 15 kV beam and 30 nA beam current.

3.3. NanoSIMS

Measurements of volatile elements including H in nominally anhydrous minerals were performed with a Cameca NanoSIMS 50L at the Carnegie Institution of Washington's Department of Terrestrial Magnetism (DTM), using methods developed by Saal et al. (2008), Hauri et al. (2011), and Mills et al. (2017). The indium sample mounts selected for NanoSIMS analysis based on electron beam pre-characterization were sputter coated with gold (~3–5 nm thick) after being briefly repolished with a dry 1 μm alumina-in-polymer lapping film to remove the carbon coat used for the initial SEM work. The samples were dried in a vacuum oven at ~50 °C before being coated with gold for NanoSIMS analysis. The samples and standards were stored for at least a day in the NanoSIMS airlock (at $\sim 10^{-8}$ torr) before being transferred into the analysis chamber. Furthermore, prior to and between the NanoSIMS sessions, the Au coated samples and standards were stored in a vacuum oven at ~50 °C in order to reduce potentially adsorbed volatiles. The abundance of H and other volatiles was then measured with the NanoSIMS in grains of nominally anhydrous minerals (alkali feldspar, plagioclase, pyroxene, and SiO_2 phases) within felsic as well as selected less-evolved assemblages. For each analysis spot, we first performed a pre-sputtering step on a 15x15 μm area for 200 seconds. For the analyses, a 2 nA primary beam of Cs^+ was rastered in a 7x7 μm area, and negatively charged ions of the isotopes ^{12}C, ^{16}OH, ^{19}F, ^{30}Si, ^{32}S, and ^{35}Cl were measured simultaneously on six electron multipliers using ion counting. Mass resolving power of the mass spectrometer was set to ~8000 in order to clearly separate $^{16}OH^-$ from $^{17}O^-$ as well as other isobaric interferences; average $^{30}Si^-$ counts for the reference ion beam were on the order of 300,000 cps. Data was acquired from the center 2.6 × 2.6 μm through beam blanking. A series of well characterized standards (n = 11) were used to determine the relative sensitivity factors for C, OH^-, F, S, and Cl (Hauri et al., 2011). A normal incident electron gun was applied to mitigate charging of the rastered area.

Using indium mounts we obtained extremely low sample chamber pressures ($\sim 4.5 \times 10^{-10}$ torr). Initially, we used the nominally anhydrous synthetic silica glass Suprasil standard to monitor the detection limits for these elements, as described in Koga et al. (2003) and Hauri et al. (2006a,b). Ultimately, we found that the Suprasil standard consistently had a greater OH^-/Si^- signal than the natural silica in lunar granite 14321,1067, equivalent to water contents of Suprasil = 2.9 ± 0.6 (2σ) ppm; granite silica = 1.5 ± 0.4 (2σ) ppm. Hence, for the instrument background we use the levels determined on the natural SiO_2 phase and this was subtracted from all analyses (Tables 2 and 3). The water content of 14321,1067 silica is therefore lower than that reported previously for lunar silica; Mills et al. (2017) found that the water content of 15405,78 silica and the Suparsil standard were indistinguishable. Qualitatively, as reported below, the difference in water content between the lunar silica phases is consistent with the difference seen in the feldspars in the two samples.

Two natural, well-characterized feldspars, adularia from Kristallina, Switzerland (Kronenberg et al., 1996), and sanidine from the Late Bishop Tuff (LV51), Long Valley, CA (Simon et al., 2008) were also measured as a check of the Relative Sensitivity Factor (RSF) curves defined by the primary standards (Table 2). The average measured water content determined for the adularia of 84 ± 2 ppm (2σ, n = 6) closely matches its known value of 79 ± 8 ppm (2σ, n = 9) and thus we see no evidence of a secondary SIMS matrix effect (e.g., Mosenfelder et al., 2015). The average measured water content for the Late Bishop Tuff sanidine (LV51) is 32.6 ± 0.9 ppm (2σ, n = 3) that has not been measured previously has a reasonable value for a terrestrial rhyolite (Johnson and Rossman, 2004).

The abundances of C, F, S, and Cl were measured along with OH^-. Similar to water (OH^-), the C, F, S, and Cl contents were found to be near or lower in the natural 14321,1062 SiO_2 phase (detection of C = 0.4 ppm; F = 0.1 ppm; S = 0.0 ppm; and Cl = 0.0 ppm) than in the Suprasil (detection of C = 0.2 ppm; F = 0.1 ppm; S = 0.0 ppm; and Cl ~ 1300 ppm). Ideally, the reported C values represent the intrinsic abundances in the unknown samples. However, C can also be found in cracks and grain boundaries at unreasonable concentrations and was therefore used in this work to identify likely analytical artifacts.

3.4. FIB-Supported FE-STEM

The regions analyzed by NanoSIMS were subsequently analyzed with field-emission scanning transmission electron microscopy (FE-STEM) to look for evidence of solid-state shock effects or shock melting in and around the NanoSIMS analysis spots, to identify the mineralogies of the SiO_2 polymorphs, and to generally characterize at the sub-micrometer scale the compositional and microstructural variations in the clasts. FE-STEM samples were prepared using lift-out focused ion beam (FIB) cross-sectioning techniques performed using a FEI Quanta dual electron/focused ion beam instrument at NASA JSC. FE-STEM imaging, nanoscale analyses, and element mapping was performed at 200 kV using the JEOL 2500SE

Table 2
Volatile abundances measured in secondary standards by NanoSIMS.

Sample	C (ppm)	H (ppm)#	F (ppm)	S (ppm)*	Cl (ppm)	Cl/F	Material	Magmatic H_2O (wt.%)**
RY-79-17		83.3	0.42	0.04	0.00	0.01	adularia	
RY-79-17	0.7	82.8	0.42	0.03	0.01	0.01	adularia	
RY-79-17		86.9	0.42	0.44	0.20	0.49	adularia	
RY-79-17	0.7	87.3	0.39	0.03	0.02	0.06	adularia	
RY-79-17	0.6	81.0	0.42	0.03	0.00	0.01	adularia	
RY-79-17		83.6	0.40	*32.86*	0.04	0.09	adularia	
Average	**0.6**	**84.2**	**0.41**	**0.11**	**0.05**	**0.11**		
LV51	0.4	31.3	0.95	0.03	0.01	0.01	sanidine	2.78
LV51	0.4	34.2	0.96	0.04	0.01	0.01	sanidine	3.04
LV51	0.4	32.3	0.96	0.05	0.02	0.02	sanidine	2.88
Average	**0.4**	**32.6**	**0.96**	**0.04**	**0.01**	**0.01**		
JSC std mount	0.0	2.1	0.10	0.02	1324	12809	Suprasil (SiO_2)	
DTM std mount	0.2	1.7	0.08	0.02			Suprasil (SiO_2)	
JSC sample mount	0.2	0.9	0.11	0.02	1301	11787	Suprasil (SiO_2)	
JSC sample mount	0.2	1.8	0.11	0.02	1265	11069	Suprasil (SiO_2)	
JSC sample mount	0.2	1.5	0.12	0.02	1400	12026	Suprasil (SiO_2)	
JSC sample mount	0.4	1.4	0.11	0.03	1298	11913	Suprasil (SiO_2)	
DTM std mount	0.1	1.1	0.08	0.03	1603	20555	Suprasil (SiO_2)	
Average	**0.2**	**1.5**	**0.10**	**0.02**	**1365**	**13360**		

* S variabiliy likely reflects contribution from mineral impurities.
** Computed magmatic H_2O content based on empirically derived distribution coefficient given by average H_2O of quartz bearing melt inclusions in LV51 (Schmitt and Simon, 2004).
# Natural SiO_2 is used to define the baseline.

FE-STEM at NASA JSC. The element mapping used a 50 mm^2 Thermo SiLi EDS detector system. Details on the protocols used can be found in Berger and Keller (2015) and Righter et al. (2015).

4. RESULTS

4.1. Volatile Abundances

The measured H abundances in our lunar feldspar samples vary from ~2 ppm to ~18 ppm (Table 3, this work and Mills et al., 2017), and are significantly less than those measured in the terrestrial adularia (~84 ppm) and sanidine (~33 ppm). The alkali feldspars measured in 14321,1062 have H contents (1.9 ± 0.6 ppm 2σ, $n = 9$) that are slightly less than the ~3–5 ppm in the mafic samples (troctolite clast from 14303, 363 and KREEP basalt from 15405, 255), and as discussed above, the abundances of H in its SiO_2 phase are so low their average was used to define the analytical background. The feldspar in the other two felsites (12013,141 and 15405,78) have H abundances that are significantly higher than feldspars in 14321,1062 and the mafic samples. Both plagioclase (6.9 ± 2.2 ppm 2σ, $n = 3$) and alkali feldspar (14.1 ± 0.8 ppm 2σ, $n = 2$) in 12013,141 and alkali feldspar (~18 ppm) in 15405,78 reported by Mills et al. (2017) are higher (Table 3). The clinopyroxene in the KREEP basalt (15405,255) yielded H abundances that are indistinguishable from the associated feldspars (both 3.6 ± 1.0 ppm 2σ, $n = 3$), while the orthopyroxene in the troctolite (14303,363) has abundances that are slightly higher (5.8 ± 0.6 ppm 2σ, $n = 3$) than its corresponding plagioclase (2.9 ± 1.0 ppm 2σ, $n = 3$) (Table 3).

The C abundances in the lunar feldspar are only slightly above background levels, except perhaps in alkali-feldspar in 12013,141 (Table 3). The F abundances in the lunar feldspars (0.2–1.4 ppm) are similar to those measured in the terrestrial feldspars. The F abundances in pyroxenes are roughly three times higher than their corresponding feldspars. The S abundances in all minerals are generally low, and the few analyses with relatively high abundances are likely due to mineral impurities. Chlorine in the lunar feldspars is also generally low and where it is relatively high it seems to be correlated with S, but these low abundance measurements are susceptible to unresolved mass interferences and further investigation is warranted.

5. COMPOSITIONAL AND MICROSTRUCTURAL RELATIONS IN NANOSIMS SAMPLES

5.1. Micrographophyre and related assemblages in 12013,141

The trace H and other volatile abundances reported for sample 12013,141 in Table 3 are from K-feldspar grains in a micrographophyre assemblage and from plagioclase grains that form an intergrowth with minor K-feldspar in contact with the micrographophyre in the same rock chip (Fig. 1). As shown in the back-scattered electron (BSE) image and RGB three-channel K-Ca-Na X-ray EDS element map in Fig. 1, the micrographophyre is modally 50 area % K-rich alkali feldspar intergrown with 50 area % of a SiO_2 phase that FE-STEM observations confirmed to be α-quartz. The quartz contains a uniform distribution of elongate-lenticular voids less than 1 μm in size that give it a "spongy" appearance in BSE images. The unfilled voids are characteristic of much of the quartz component of the 12013 micrographophyre and have also been described by Quick et al. (1981) and Seddio et al. (2015). A few pyroxene grains 10–20 μm in size occur around the outer margin of

Table 3
Volatile abundances measured in lunar mineral phases by NanoSIMS.

Sample	C (ppm)	H (ppm)#	F (ppm)	S (ppm)*	Cl (ppm)	Cl/F	Material	Magmatic H_2O (wt%)**
15405,255	0.6	4.5	0.85	0.03	0.01	0.01	plagioclase	0.11
15405,255	0.8	4.3	0.84	0.08	0.06	0.07	plagioclase	0.11
15405,255	2.1	5.4	0.74	0.03	0.01	0.02	plagioclase	0.14
15405,255	1.1	3.8	0.87	0.04	0.03	0.04	plagioclase	0.10
Average	**1.2**	**4.5**	**0.83**	**0.05**	**0.03**	**0.03**		**0.11**
14321,1062	0.5	2.0	0.38	3.19	2.26	6.01	alkali feldspar	0.20
14321,1062	0.4	1.8	0.60	0.03	0.02	0.03	alkali feldspar	0.18
14321,1062	0.4	1.9	0.41	0.03	0.06	0.14	alkali feldspar	0.19
14321,1062	1.4	2.5	0.58	0.08	0.04	0.07	alkali feldspar	0.25
14321,1062	0.4	1.9	1.32	0.06	0.30	0.22	alkali feldspar	0.19
14321,1062	0.8	1.6	0.58	0.03	0.02	0.04	alkali feldspar	0.16
14321,1062	0.7	1.5	1.00	2.96	3.27	3.26	alkali feldspar	0.15
14321,1062	0.7	1.5	1.05	11.85	4.67	4.46	alkali feldspar	0.15
14321,1062	0.8	2.1	0.58	0.03	0.05	0.09	alkali feldspar	0.21
Average	**0.7**	**1.9**	**0.72**	**2.03**	**1.19**	**1.59**		**0.19**
14321,1062	0.3	0.1	0.09	0.03	0.00	0.04	SiO_2	
14321,1062	0.6	0.3	0.10	0.02	0.06	0.61	SiO_2	
14321,1062	0.3	−0.1	0.12	0.02	0.00	0.02	SiO_2	
14321,1062	0.2	−0.2	0.11	0.03	0.00	0.04	SiO_2	
Average#	**0.3**	**0.0**	**0.10**	**0.02**	**0.02**	**0.18**		
15405,255	1.7	3.0	3.48	0.31	0.01	0.00	clinopyroxene	
15405,255	1.8	3.6	3.91	0.70	0.01	0.00	clinopyroxene	
15405,255	0.7	4.0	1.86	0.14	0.14	0.08	orthopyroxene	
Average	**1.4**	**3.6**	**3.08**	**0.38**	**0.05**	**0.03**		
14303,363	0.6	3.5	1.35	0.19	0.61	0.45	plagioclase	0.09
14303,363	0.7	2.7	1.73	0.06	1.61	0.93	plagioclase	0.07
14303,363	0.6	2.4	1.10	0.37	1.54	1.40	plagioclase	0.06
Average	**0.6**	**2.9**	**1.39**	**0.2**	**1.3**	**0.9**		**0.07**
14303,363	1.2	5.5	4.38	0.10	0.30	0.07	orthopyroxene	
14303,363	1.3	5.9	3.68	2.09	0.13	0.03	orthopyroxene	
14303,363	1.1	6.1	3.58	0.04	0.01	0.00	orthopyroxene	
Average	**1.2**	**5.8**	**3.88**	**0.74**	**0.15**	**0.04**		
12013,141 Clast 11	0.6	6.7	0.13	0.08	0.11	0.87	plagioclase	0.67
12013,141 Clast 11	0.5	5.9	0.76	0.04	0.45	0.59	plagioclase	0.59
12013,141 Clast 11	0.5	8.1	0.14	0.09	0.14	1.01	plagioclase	0.81
Average	**0.5**	**6.9**	**0.34**	**0.07**	**0.24**	**0.83**		**0.69**
12013,141 Clast 11	4.4	14.7	0.16	0.08	0.14	0.87	alkali feldspar	1.47
12013,141 Clast 11	3.8	13.5	0.18	0.09	0.08	0.46	alkali feldspar	1.35
Average^	**4.1**	**14.1**	**0.17**	**0.09**	**0.11**	**0.67**		**1.41**

* S variabiliy likely reflects contribution from mineral impurities.
** Computed range of magmatic H_2O content assuming $D = 0.001$ (evolved melt) and 0.004 (primitive melt), respectively.
# Natural SiO_2 is used to define the baseline.
^ C is high in these alkali-feldspar analyses, SEM imagery shows no evidence that ion beam hit cracks or grain boundaries.

the microgranophyre (Fig. 1). Looking at the microstructural relations of the pyroxene relative to the microgranophyre, however, it is unclear whether the pyroxene is part of the primary microgranophyre assemblage, or whether they represent juxtaposed components from the surrounding breccia matrix.

The microgranophyre has the "trellis" or "herringbone" microstructure of interlocking semi-skeletal quartz and feldspar grains that typifies the patchy microgranophyre regions in the 12013 gray breccia (Quick et al., 1981). EPMA analyses plotted in Fig. 2a show that the normalized compositions of the microgranophyre alkali feldspar varies from $Or_{73}Ab_{22}An_2$ with 1.6 wt.% BaO to $Or_{60}Ab_{26}An_{14}$ with 1.4 wt.% BaO. These compositions are consistent with the trends shown in the larger dataset of microgranophyre alkali feldspar composition that we acquired for comparative purposes from other areas of microgranophyre in our available 12013 sample suite (Fig. 2a). Full details of this larger dataset are discussed below.

The plagioclase/K-feldspar intergrowth features seen in contact with the microgranophyre represent a polycrystalline assemblage modally dominated by 95 area % plagioclase of varying An content with approximately 5 area % K-feldspar. Similar to the microgranophyre, pyroxene grains occur around the intergrowth's outer margin but are not clearly interpretable as part of the intergrowth assemblage itself. Composite K-Ca-Na EDS X-ray maps show higher- and lower-An content regions inside the plagioclase, with K-feldspar occurring in irregularly shaped enclaves mostly in the interior portions of the assemblage

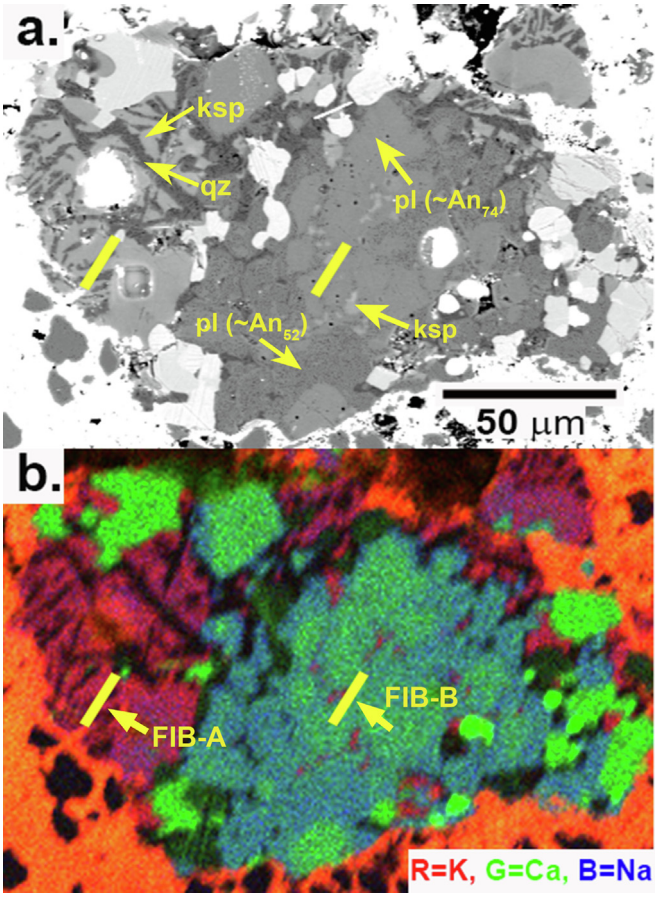

Fig. 1. FE-SEM back-scatter electron image (a) and X-ray EDS three-channel composite K, Ca and Na element map (b) of rock fragment from lunar breccia sample 12013,141. NanoSIMS trace volatile data were obtained on K-feldspar within the granite micrographophyre making up the left side of the fragment, and on plagioclase from the intergrowth of plagioclase with minor K-feldspar that occurs on the right side of the fragment. Yellow lines show the locations of FIB lift-out cross section prepared for FE-STEM characterization.

(but some areas are around the aggregate margin) (Fig. 1a, b). EPMA compositions for the higher- and lower-An plagioclase areas are plotted in Fig. 2a, and correspond to average compositions of An_{74} and An_{52}, respectively. The K-feldspar enclaves are too small and microstructurally complex to measure reliably by EPMA, but a grain within the enclave was determined to have a normalized composition of $Or_{78}Ab_{15}An_7$ (with ~3.0 wt.% BaO) based on FE-STEM EDS analyses discussed below (Fig. 2a). From the relatively brighter BSE contrast of the An_{74} plagioclase grains (distinctly brighter green color in the composite EDS map; Fig. 1a,b), the intergrowth exhibits an overall microstructure characterized by what looks to reflect relict, more chemically homogeneous, individual grains of ~An_{74} plagioclase, enclosed in a finer-grained, less-homogeneous, assemblage made up of the ~An_{52} plagioclase and the minor ~Or_{78} K-feldspar in the enclaves.

FIB samples for FE-STEM characterization were prepared along one cross-section in the micrographophyre and another in the plagioclase/K-feldspar intergrowth as indicated in Fig. 1. In the BSE image of the micrographophyre FIB sample in Fig. 3a, the quartz and K-feldspar exhibit a geometrically complex interpenetrating microstructure with elongate and curving-to-bulging grain boundaries. The bright-field conventional TEM image in Fig. 3b shows additional details about the size and shape of the previously-described voids in the quartz. This and other TEM images did not reveal any secondary phases filling the voids or lining their walls (Fig. 3b). Selected-area electron diffraction patterns of the quartz regions consistently indexed with an exact match for α-quartz. The quartz regions are polycrystalline and made up of sub-grains 0.50–0.75 µm in size that generally have low densities of dislocations or other defects associated with structural strain (Fig. 3). A few quartz grains were found that exhibit localized lamellar defects that are likely twins (Fig. 3). Fig. 3 also shows that as with the quartz, the K-feldspar in the micrographophyre assemblage has a low defect density and is fully crystalline. FE-STEM quantified EDS scanned-probe analyses of the K-feldspar yield compositions that plot along the same ternary composition trend as the EPMA analyses acquired on other alkali feldspars from the 12013 micrographophyre (Fig. 2b).

Conventional bright-field TEM images of the plagioclase/K-feldspar intergrowth show that it is made up of grains with complex curvilinear-to-embayed shapes

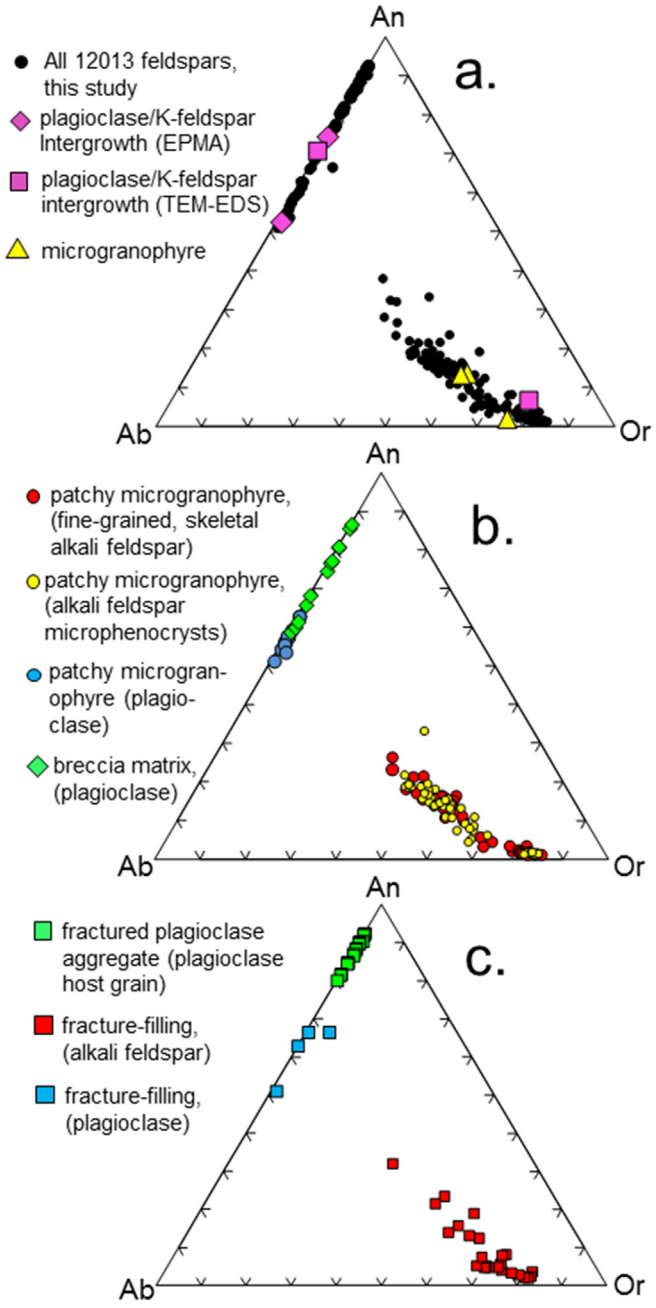

Fig. 2. Feldspar compositions in felsite clasts from lunar breccia 12013. All analyses by EPMA except as noted. (a) Color symbols show compositions of feldspars in microgranophyre and plagioclase/K-feldspar intergrowths in sample 12013,141 (diamonds, squares, triangles) for which NanoSIMS trace volatile measurements are reported. Black symbols show entire compositional dataset of 12013 feldspars measured in current study for comparison. (b) Feldspars in patchy microgranophyre regions and surrounding breccia matrix in 12013,167 rock chip samples. (c) Compositions for fractured plagioclase and associated fracture-filling assemblage of alkali feldspar and intermediate plagioclase in 12013,167 rock chip samples. All feldspar compositions are reported in Table S1-Supplemental Materials.

that are similar to those found in the microgranophyre (Fig. 4). Compared to the microgranophyre, however, the grains in the plagioclase/K-feldspar assemblage have a much higher concentrations of strain-related defects, including dislocations and low-angle subgrain boundaries (Fig. 4). Details of this defect substructure are particularly visible in Fig. 4b, which was acquired with the sample tilted into a maximum strain contrast diffraction orientation. The plagioclase contains regions with variable dislocation densities that are in turn separated by both low- and high-angle grain boundaries. The K-feldspar grain with the embayed shape in Fig. 4a and b is part of one of the small enclave-like K-feldspar regions transected by the FIB section line in Fig. 1. Quantified FE-STEM scanned beam EDS

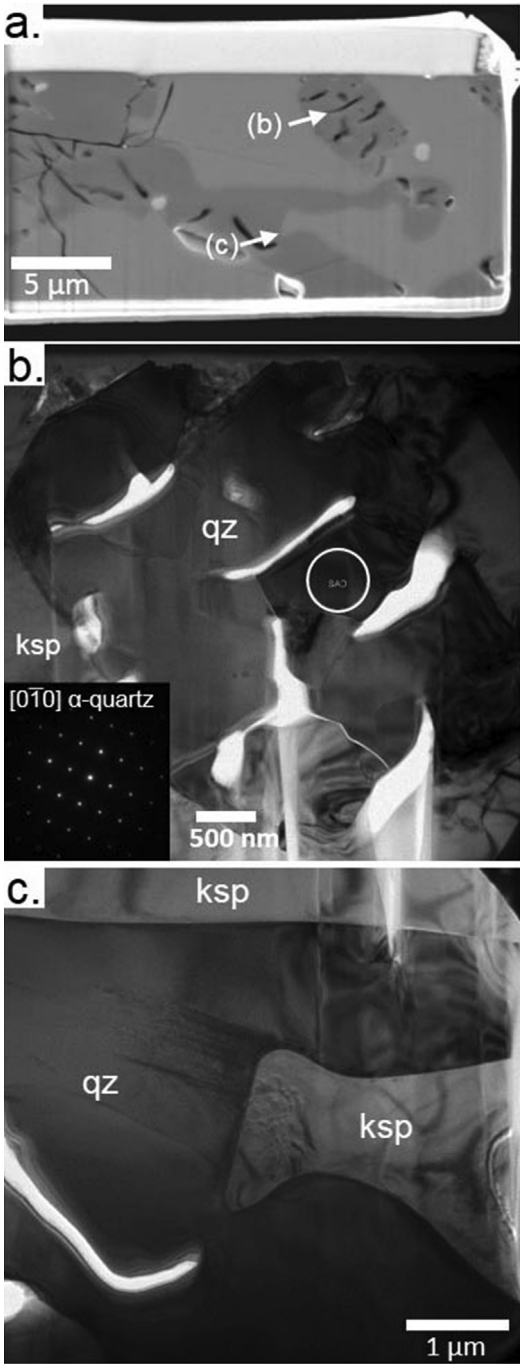

Fig. 3. SEM back-scattered electron image of FIB cross-section (prior to final ion milling) extracted from FIB-A location in 12013,141 micrographyre shown in Fig. 1(a). Arrows show locations corresponding to the conventional TEM bright field images in (b) and (c). In (b) the grain in dark diffraction contrast is identified as α-quartz based on the selected-area electron diffraction pattern (inset) aquired from region outlined by white circle (pattern indexing based on trigonal unit cell). In both the SEM image in (a) and the TEM image in (b), the quartz exhibits the vermiform-lenticular voids characteristics of much of the quartz occurring in the 12013,141 micrographyre intergrowths. The TEM bright-field image in (c) details the complex re-entrant morphology of grain boundaries between quartz and K-feldspar in the micrographyre.

analyses of this grain yield a normalized composition of $Or_{78}Ab_{15}An_7$ (with ~3.0 wt.% BaO) as plotted in Fig. 2a. The plagioclase grains in contact with the K-feldspar in Fig. 4 are similar to one another in composition, averaging $An_{70}Ab_{30}$ as measured by FE-STEM EDS. This composition agrees with the compositions of the calcic plagioclase in the intergrowth determined by EPMA (Fig. 2a).

5.2. Micrographyre 14321,1027

The H and other trace volatile abundances reported for sample 14321,1062 in Table 3 were measured on multiple K-feldspar grains and SiO_2 grains from the 14321,1062 mineral separate prepared by Shih et al. (1985) using chips from the parent granite clast 14321,1027 (Warren et al., 1983) (Table 1). A FE-SEM BSE image and EDS K and Al element maps for one of the analyzed K-feldspars (1.5–1.6 ppm H, Table 3) is shown in Fig. 5. The FE-SEM imaging and analytical results show that, on the micrometer scale at least, the grain is a single-phase with a high degree of compositional homogeneity (i.e., no zoning). A quantified EDS spectrum extracted for the bulk grain from an SEM EDS compositional spectrum image yielded a normalized composition of $Or_{92.5}Ab_{5.5}An_{2.1}$ with 0.60 wt.% BaO (Fig. 6). Additional quantified EDS spot analyses yielded varying intra-grain compositions of Or_{88-92} (Fig. 6). This range of compositions overlaps with the larger set of EPMA analyses we obtained on K-feldspars in thin sections containing other fragments of the 14321,1027 granitic clast (Fig. 6). To investigate the microstructure of the Fig. 5 K-feldspar grain to look for sub-micrometer structural defects possibly associated with shock, a FIB lift-out section was prepared for FE-STEM characterization (Fig. 7). The section was made after the NanoSIMS analyses were performed and was removed from an area of the grain separated by at least 10–20 micrometers from the edges of the sputtered NanoSIMS pits. Conventional bright-field TEM imaging confirmed that the sectioned portion of the grain was a single crystal with relatively featureless bright-field electron diffraction contrast except for local microcracks directly below the sample's original polished surface (Fig. 7). Selected-area electron diffraction patterns in several different zone axis orientations indexed consistently with an exact match for end-member K-feldspar. These patterns were not, however, diagnostic as to the degree of structural state Al-Si ordering in the sample due to inherent limitations in electron diffraction for assessing this parameter compared to X-rays. Distortional strain contrast effects in conventional and high-resolution TEM imaging, as compared to electron diffraction, have been used to find evidence of partial Al-Si order in some intermediate structural state K-feldspars (McConnell, 1965, 1971). These effects were looked for in the current samples in zone axis orientations for which they have been reported, but were not observed.

A FE-STEM characterization study was also performed after NanoSIMS analysis on one of the 14321,1062 SiO_2 grains (−0.2 ppm H, Table 3). Multiple selected-area electron diffraction patterns of the grain confirmed it to be single-crystalline α-quartz. Similar to the 14321 K-feldspar

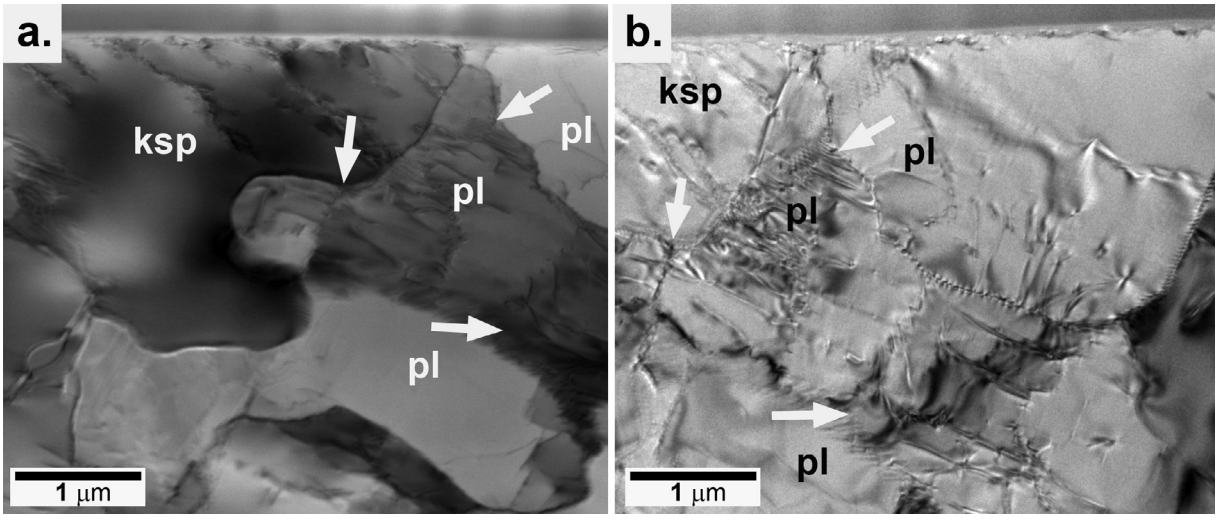

Fig. 4. Bright-field STEM (a) and conventional TEM (b) images of area within FIB-B cross section taken from polycrystalline plagioclase + K-feldspar intergrowth in 12013,141 (see Fig. 1). The K-feldspar grain (ksp) marked in (a) is part of one of the small K-feldspar enclaves that show up as reddish patches in Fig. 1b. Image (b) shows a region slightly to the right of (a) with arrows marking the same spots in both images. Image (b) was taken in conventional TEM bright-field imaging mode with the sample diffraction orientation adjusted to increase visibility of low-angle grain boundaries, dislocations and other defects.

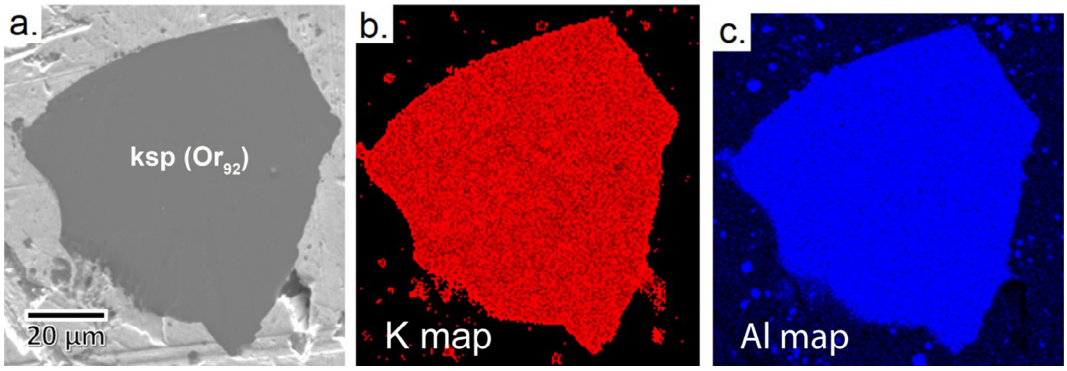

Fig. 5. SEM BSE image of NanoSIMS-analyzed K-feldspar grain from 14321,1062 grain separate taken prior to NanoSIMS analysis for trace volatiles (a). SEM EDS X-ray count element maps for K (b) and Al (c) of grain in (a). Pixel intensity versus X-ray count scaling identical in both element maps.

grain (Fig. 7a), conventional bright-field TEM images showed featureless diffraction contrast, with no dislocations or other defects (Fig. 7b).

5.3. Glassy microgranophyre 15405,78

For comparison to the current set of trace H and other volatile measurements, Table 3 includes the average value for H data previously reported by Mills et al. (2017) for measurements in several microgranophyre clasts in a mm-size rock chip from lunar breccia 15405,78. To optimize our understanding of the context of the Mills et al. (2017) data relative to our new results, we carried out an expanded EPMA, FE-SEM and FE-STEM study of the clasts from Mills et al. (2017), as well as of other similar microgranophyre clasts in the 15405,78 sample chip. An FE-SEM BSE image and RGB three-channel K-Ca-Na X-ray EDS element map for the main Mills et al. (2017) clast are shown in Fig. 8. The clast is modally 40 area % SiO_2 that forms a lamellar/irregular microgranophyric intergrowth with 60 area % of a K-rich feldspathic phase. EPMA analyses of the feldspathic phase in the Fig. 8 clast, and several other similar clasts in the 15405,78 rock chip, consistently yielded feldspar 8-oxygen formula totals significantly less than 1 for the A-site cations (Na + K + Ca + Ba), despite near 100 wt.% oxide totals and T-site (Si + Al) cation totals near 4. Variation in the A- to T-site cation proportions for the analyses as plotted along a stoichiometric anorthite + celsian versus albite + K-feldspar join is shown in Fig. 9.

For general characterization purposes as well as to resolve the non-stoichiometry problem in the EPMA analyses, a FIB section for FE-STEM characterization was prepared from the Mills et al. (2017) clasts along the transect shown in Fig. 8, which contained a lamellar SiO_2 region bounded on both sides by feldspathic material (Fig. 8). In

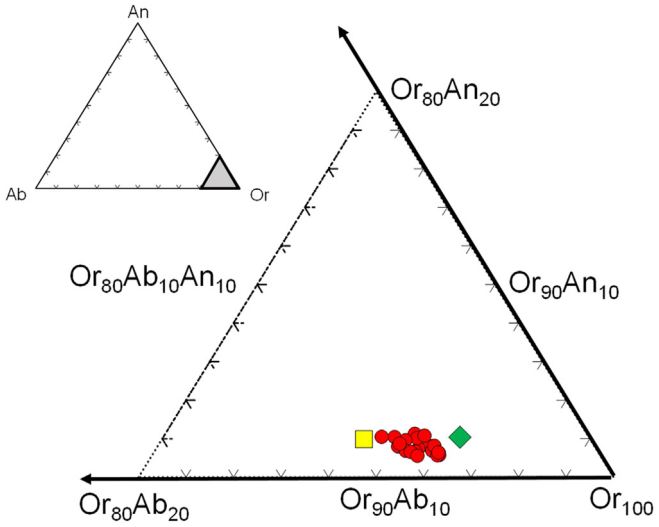

Fig. 6. Ternary compositions of K-feldspars in granitic clasts in lunar breccia 14321 as measured in this study (red and green symbols) and compared to the average composition reported for K-feldspar in 14321,1027 granite clasts by Warren et al. (1983) (yellow symbol). Green diamond symbol is the bulk composition of the 14321,1062 K-feldspar grain shown in Fig. 5, and for which the trace H content is reported in Table 3. Red symbols plot compositions measured by EPMA in the current study for K-feldspars in granite clasts within lunar 14321 thin sections 14321,149; 14321,1494 and 14321,993.

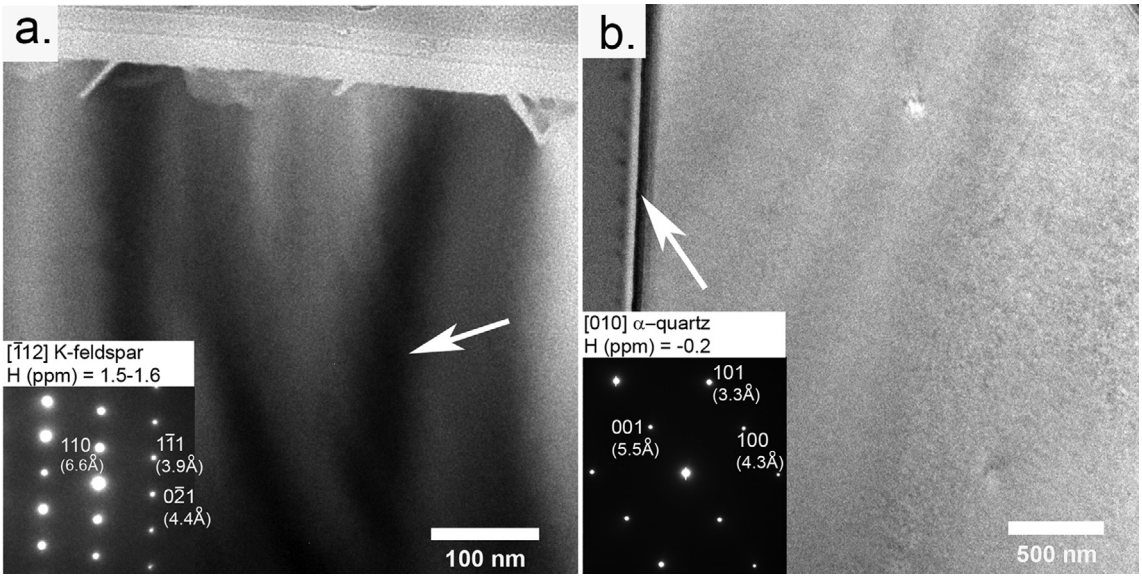

Fig. 7. Conventional TEM bright-field images and corresponding selected-area electron diffraction patterns of FIB-sectioned K-feldspar (a) and α-quartz (b) grains from sample 14321,1062. Both grains were prepared for NanoSIMS analysis from the Shih et al. (1985) 14321,1062 mineral separate sample (see text). The ppm H contents indicated on each figure correspond to values listed in Table 1. The FIB sections were prepared after NanoSIMS analyses were performed, but were taken from areas well separated from sputtered regions. The dark band designated by the arrow in (a) is a bend contour diffraction contrast feature not associated with any type of crystalline defect. The arrow in (b) points to the boundary between the grain and the protective carbon FIB strap layer. The electron diffraction patterns corresponding to each image list the measured *d*-spacings for the indexed reflections. Three-axis (trigonal) indexing is used for the α-quartz diffraction pattern.

the BSE images of the FIB section prior to final ion milling, the feldspathic regions appear as bright contrast "feathery" materials intergrown with a darker-contrast matrix (Fig. 10). TEM images, EDS analyses, and electron diffraction confirm that the darker-contrast matrix is feldspathic glass, whereas the brighter material is composed of skeletal crystallites of SiO_2-tridymite 50–250 nm in size hosted in 10–20 area % feldspathic glass (Fig. 10). In addition to the tridymite crystallites, electron diffraction confirmed that the SiO_2 lamellar region in the center of the transect is also made up of tridymite, in the form of lath-shaped crystals 0.5–0.7 μm in size (Fig. 10).

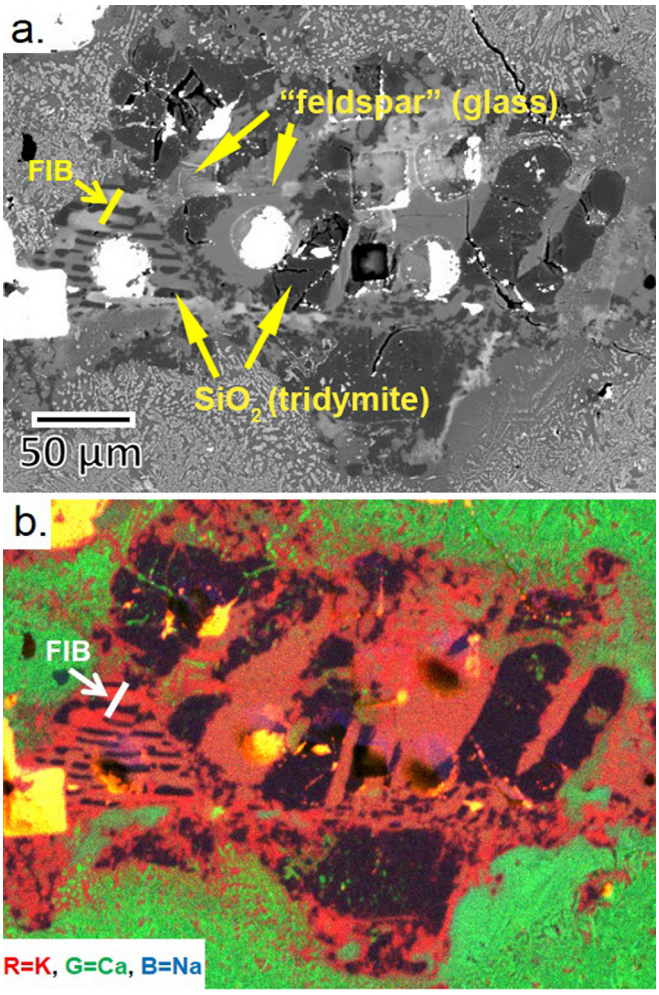

Fig. 8. FE-SEM BSE image (a) and corresponding RGB three-channel K-Ca-Na EDS X-ray element map (b) of 15405,78 microgranophyre clast whose trace volatile contents were previously measured by Mills et al. (2017). Previous ion probe analysis pits can be seen. RGB color channel pixel intensity versus X-ray count scaling is identical for all three elements. Arrows point to location of FIB cross-section transect.

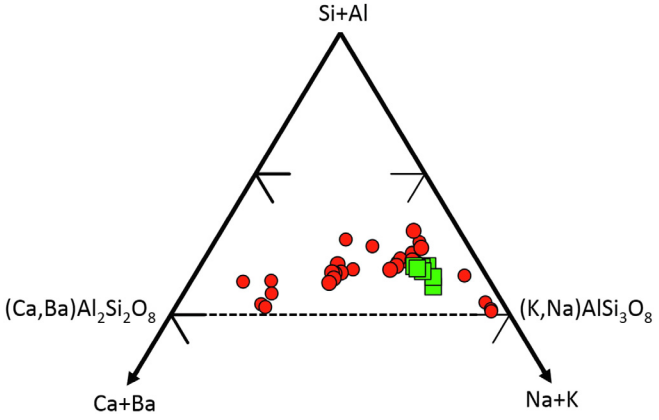

Fig. 9. Compositions of feldspathic regions in microgranophyric clasts within lunar breccia 15405,78 measured in the current study by EPMA and plotted with respect to the atomic percentages of the cation components (Ca + Ba), (Si + Al) and (Na + K). Dashed line is the compositional join expected for stoichiometric feldspar. Green squares are compositions of feldspathic regions in the larger of two clasts previously measured by Mills et al. (2017) that contain ~18 ppm H_2O. Red circles are compositions of feldspathic regions in additional clasts in the 15405,78 rock fragment studied by Mills et al. (2017).

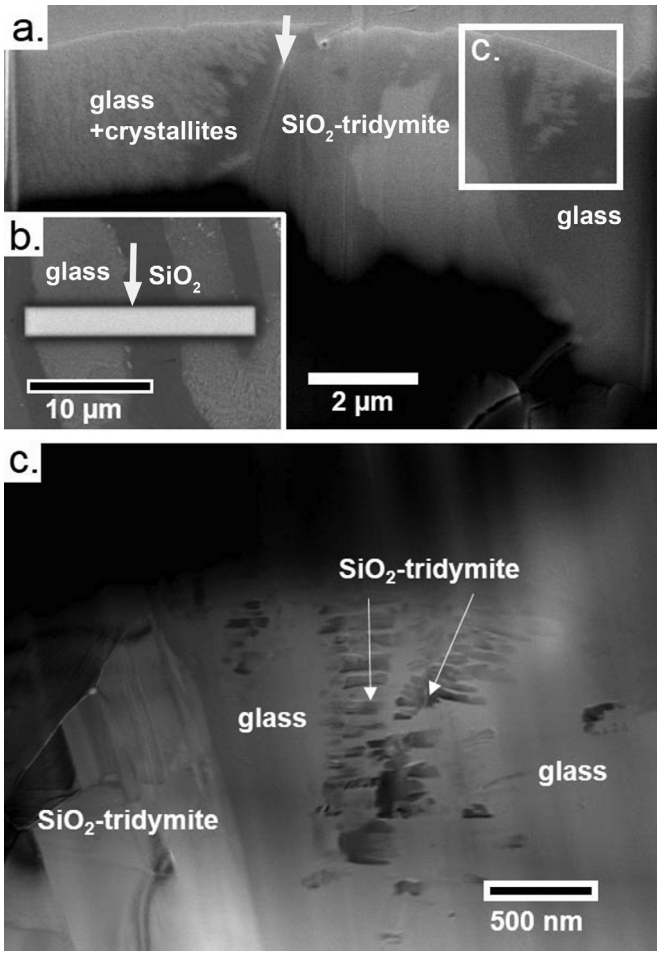

Fig. 10. BSE image of FIB cross-section extracted along the FIB transect 15405,78 shown in Fig. 8 and taken before final ion milling (a). BSE image showing exact positioning of the FIB section protective "strap" layer in relation to SiO_2 and feldspathic "fsp" phases across the FIB transect (b). The left-to-right orientation of images (a) and (b) are the same, with a white arrow used to show the position of the same grain boundary in both images. Conventional TEM bright-field image (c) of the region outlined by the white inset box in image (a).

5.4. Mafic clasts 15405,255 and 14303,363

Table 3 reports additional trace volatile measurements made on plagioclase, pyroxenes, and olivine in lithic clasts with less-evolved affinities from parent breccias 15405 and 14303. Sample 15405,255 consisted of mm-sized chip fragments derived from a parent clast (15405,93) that was originally allocated to the 1976 Imbrium Consortium (Adams et al., 1976) but never studied in detail. It was only macroscopically described by them as a "large white clast" that had separated from the parent breccia during sawing. Despite the clast's white color, our FE-SEM study of the 15405,255 fragments showed them to be a homogenous mafic assemblage containing roughly 50 area % plagioclase (An_{85-88}), 30 area % orthopyroxene (Di_{3-5}, En_{80-82}, Fs_{20-23}), and a total remaining modal percentage of 5–10 area % composed of olivine (Fo_{75-76}) and clinopyroxene (Fig. 11). K-feldspar (Or_{85-95} with 2.0–3.0 wt.% BaO) also occurs as a minor phase in intergrowths with the matrix plagioclase (Fig. 11). The assemblage has a distinctive fine-grained (<100 µm) equigranular texture (Fig. 11). Although the 15405,255 assemblage is overall basaltic in character, its texture, modal composition and mineral chemistries distinguish it from the majority of 15405 lithic clasts described in the literature (Ryder, 1976; Ryder and Martinez, 1991). The latter are dominated by variously textured KREEP basalts with no resemblance to the current 15405,93,255 material, and QMD/granite felsite clasts, of which the 15045,78 microgranophyres described in the current study are one set of examples. The possibility that 15405 might contain a heretofore un-documented population of light-colored but mafic clasts possibly related to 15405,93,255 is suggested by descriptions in Ryder (1976), in the Imbrium Consortium report (Adams et al., 1976), and by Lindstrom et al. (1988), but will require further work to confirm.

Sample 14303,363 derives from an allocation of white-to-light-colored rock chips produced during a wire saw cut of parent rock 14303,7 (Table 1; Meyer, 2016). The 14303,363 data in Table 3 are for olivine and plagioclase grains that dominate the assemblage of one of these chips after it was disaggregated by further chipping and

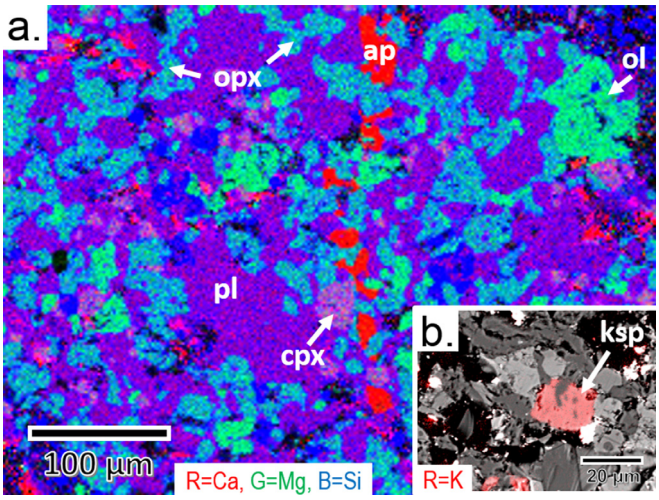

Fig. 11. Analytical FE-SEM composite element map (a) and BSE image (b) of mafic igneous assemblage from sample 15405,255 for which plagioclase and pyroxene trace volatile contents are reported in Table 2. (a) RGB color composite EDS X-ray element map with R = Ca counts, G = Mg counts and B = Si counts. Linear scaling of color channel pixel intensities (0–255) versus X-ray counts is the same for all three elements. (b) Gray scale BSE image overlaid with K (potassium) X-ray counts in red color channel showing occurrence of minor K-feldspar in a mesostasis-like intergrowth with plagioclase.

transferred to a polished indium grain mount. The mount assemblage consists of approximately 60 area % plagioclase and 40 area % olivine grains, both having a comparatively coarse grain size of 100–500 µm. No isolated grains of pyroxene of comparable grain size to the olivine and plagioclase were found. A minor amount (<5 area %) of much finer grained basaltic lithic fragment material was also identified. Although the plagioclase and olivine largely occur as separated grains on the mount, some attached grains were identified, suggesting that the grains are from a shared parent assemblage, most likely a troctolite. Quantified EDS analyses showed the olivine compositions to be in a relatively narrow range between $Fo_{87\text{-}85,}$ which agrees well with the range of olivine compositions reported for troctolite clasts in 14303 and other Apollo 14 breccias by Warren and Wasson (1980). The analyzed plagioclase compositions of $An_{85\text{-}95}$ are slightly more sodic and variable than the Warren and Wasson (1980) troctolite plagioclases, but are still in agreement within analytical error.

6. EXPANDED CHARACTERIZATION OF FELSITE MATERIAL

The highest measured H abundances for the felsite samples in the current study are for the feldspathic domains in the 15405,78 microgranophyre (~18 ppm, Mills et al., 2017), followed by feldspars in the microgranophyre and neighboring plagioclase/K-feldspar intergrowth in 12013,141 (6.9–14.1 ppm H), and finally by K-feldspar from the 14321,1062 granitic clast sample (1.9 ppm H). As previously noted, our FE-STEM results have confirmed that the feldspathic domains in the 15405,78 microgranophyre studied by Mills et al. (2017) are in fact not crystalline feldspar, but feldspathic glass that deviates substantially from normal feldspar stoichiometry, averaging only 0.75 atoms of (Ca + Ba + Na + K) per 4 of (Si + Al). This characteristic sets 15405,78 uniquely apart from the crystalline felsite assemblages in the other samples, and the implication of this difference for interpreting the H content of the 15405,78 assemblage is discussed in full detail in a later section.

Additional samples of the 14321,1062 and 12013,141 felsite assemblages, which are wholly crystalline but significantly different in microstructure and feldspar composition, were studied to expand our understanding of their differences beyond descriptions already available in the literature (e.g., Quick et al., 1981; Warren et al., 1983). For 14321,1062 this additional work involved FE-SEM and EPMA characterization of 14321,1062 granitic clasts contained in thin section 14321,993 previously studied by Warren et al. (1983) and thin sections 14321,1493 and 14321,1494 previously studied by Meyer and Yang (1988). For 12013 we studied felsite-containing rock chips 0.4–0.5 mm in size from an allocated group of rock fragments designated 12013,167 (Table 1). Similar to the 12013,141 NanoSIMS sample, these chips were identified as coming from gray as opposed to dark breccia areas on the walls of a saw cut piece (Table 1).

EPMA analyses of K-feldspars in thin sections of the 14321,1493 and ,1494 granite clasts yielded a narrow range of compositions between $Or_{89\text{-}92}$ with 0.3–0.5 wt.% BaO (Fig. 6). The quantified FE-SEM EDS analysis for the 14321,1062 mineral separate grain, measured by NanoSIMS, plots close to this range within error (Fig. 6). The average 14321,1027 K-feldspar composition reported by Warren et al. (1983) is slightly less sodic, but this may reflect relative difference in Na volatilization between the EPMA analytical procedures (Fig. 6). Our EPMA results are, however, in overall good agreement with previous studies in showing relatively limited compositional variation in the 14321,1062 K-feldspar, including a lack of rim-to-core compositional zoning in individual grains. As imaged in

FE-SEM, individual intact granitic clasts in the ,1493 ,1494 and ,993 thin sections are 0.2–0.3 mm in size (with some as large as 1.3 mm) and are composed of approximately 60 area % K-feldspar, 40% area quartz with traces of other phases as described by Warren et al. (1983) (A representative BSE image of the ,1494 thin section is shown in Meyer and Yang, 1988 and is not reproduced here). The K-feldspar and quartz share curvilinear, re-entrant/interpenetrating grain boundaries, e.g., a "micrographic" texture as described by Warren et al. (1983) and have similar grain sizes in the range of 0.2–0.5 mm. Whereas previous studies of the 14321,1062 granitic clast material have tended to emphasized the characteristics of larger, intact clasts, it should be noted that these made up only 20–30% of the clast population in the thin sections we studied, with the rest being individual K-feldspar and quartz grains surrounded by matrix. In FE-SEM BSE images the matrix has a uniform < 5 μm grain size, and is (micro) crystalline with a modal composition and texture as described by Lally et al. (1972).

FE-SEM and EPMA characterization of the two 12013,167 rock chips were directed at locating and studying larger additional areas of material similar to the samples used for the NanoSIMS measurements, specifically areas of microgranophyre as well as any regions that might show similarities to the K-feldspar + plagioclase intergrowth. As revealed by composite Na-Ca-K X-ray element maps, both chips were found to contain approximately 20–25 area % of irregularly distributed patches of microgranophyre 10–50 μm in size, enclosed in more mafic, wholly-crystalline, host material modally dominated by plagioclase and pyroxene (Fig. 12a). The mafic host matrix material is a microstructurally diverse assemblage of mostly angular fragmental mineral clasts of pyroxene and plagioclase, with some igneous-textured mafic lithic clasts. The matrix plagioclase is predominantly An_{80-90} in composition, but a significant 10–20 area % of single grains and texturally-diverse aggregates of intermediate plagioclase An_{50-65} also occur.

The microgranophyre patches in the 12013,167 chips display the same trellis/herringbone-like intergrowth of quartz with semi-skeletal, compositionally inhomogeneous alkali feldspar as in the 12013,141 NanoSIMS sample (Figs. 1 and 12). The 10–20 μm grain-size of the alkali feldspar within these fine-grained intergrowths was large

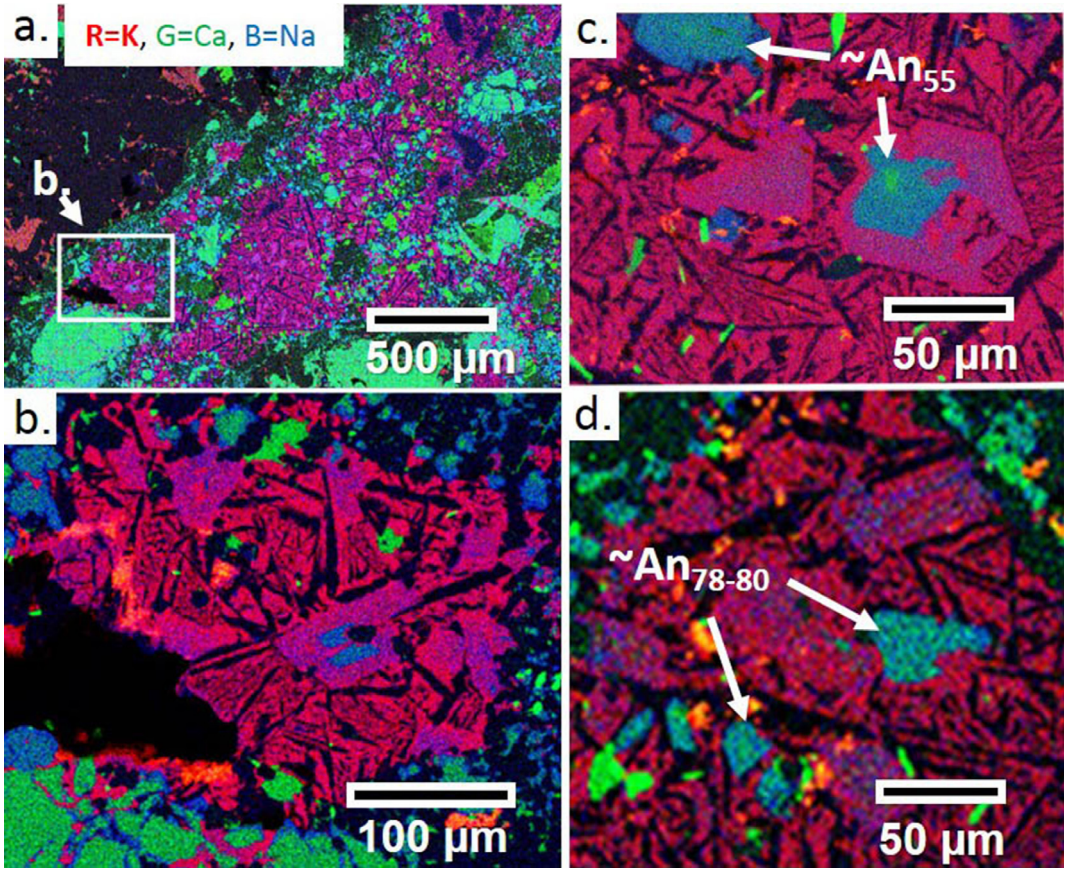

Fig. 12. Analytical FE-SEM EDS X-ray count composite K, Ca and Na element maps of patchy microgranophyre regions in sample 12013,167. RGB 8-bit color channels have R = K counts, G = Ca counts, and B = Na counts. Scaling of B = Na channel is slightly increased to enhance visibility of regions of intermediate plagioclase (blue) relative to alkali feldspar (red) and more calcic plagioclase (green). Typical size, shape and distribution of microgranophyre patches (pink/red) relative to breccia matrix assemblages (green and blue) is shown in (a). Interior detail of microgranophyre patches in (b-d) shows alkali feldspar microphenocrysts, some with cores of intermediate plagioclase as well as isolated grains of intermediate and calcic plagioclase. (For interpretation of the references to colour in this figure legend, the reader is referred to the web version of this article.)

enough for reliable quantitative EPMA analysis to be obtained (Fig. 2a and b). On the feldspar ternary composition plot in Fig. 2b, the data show a well-defined continuous trend extending from Or_{75-85} with little or no anorthite (An) component, to ternary compositions enriched in both albite (Ab) and An components up to the range of $Or_{50}Ab_{25}An_{25}$. As previously noted, analyses obtained for the alkali feldspars in the 12013,141 NanoSIMS sample fall within this trend (Fig. 2a and b).

Although there is an essential resemblance in microstructure, modal mineralogy and mineral compositions between the microgranophyre region in the 12013,141 NanoSIMS sample, and microgranophyre patches in the larger 12013,167 breccia chips, the larger microgranophyre patches in the 12013,167 chips contain additional features of note not seen in the (smaller) 12013,141 fragment. These include the presence, in most microgranophyre patches, of scattered subhedral to euhedral phenocryst-like alkali feldspar grains with larger grain size (100–200 μm) than the enclosing assemblage (Fig. 12). Several of these microphenocrysts (as they will be referred to here) have compositionally distinct interior cores made up of An_{50-65} plagioclase containing little or no K (Fig. 12c and d). Aside from these grain cores, however, EDS mapping and EPMA analyses show the microphenocrysts have intra-grain and inter-grain compositional trends overlapping that of the finer-grain alkali feldspars in the microgranophyre matrix (Fig. 2b).

In addition to the microphenocrysts, the microgranophyre patches also contain 2–5 area % scattered grains of two distinct compositional populations of plagioclase (Fig. 12). The first set of these are anhedral grains 20–100 μm in size typically found interstitial to the microgranophyre matrix grains. They have the same An_{50-65} range of composition as the plagioclase cores in the alkali feldspar microphenocrysts. The second set of grains are of similar size, anhedral in shape and also interstitial to the matrix feldspar and quartz grains, but have an An_{80-90} range of composition that is distinctly more calcic (Fig. 12d). This latter range matches that of the predominant plagioclase composition occurring with pyroxene in the host breccia matrix surrounding the microgranophyre patches.

A key overall attribute of the microgranophyre patches is the complex way the feldspathic material of a given patch interpenetrates adjacent intergranular spaces of surrounding breccia matrix. Fig. 12b shows a typical area next to a microgranophyre patch where Na- and/or K-enriched material forms μm-scale vein-like structures associated with fractures and/or irregular void spaces. Although the smaller-scale examples of these features generally do not contain a silica phase, wider fractures or voids (e.g., 30–50 μm) may also contain silica. In addition, we characterized multiple examples where fractured areas of matrix not visibly connected to microgranophyre patches also contained interpenetrating feldspathic material. Many of these involve fracture networks in single grains or grain aggregates of coarser-grained, calcic matrix plagioclase in which the fracture space is filled by a K-feldspar + plagioclase + minor silica assemblages that is similar to material found inside fracture networks within the breccia matrix (Fig. 13). EPMA analyses confirm a stoichiometric range of compositions for the K-rich feldspar that is similar to that of alkali feldspar in the microgranophyre patches (Fig. 2). The plagioclase has an intermediate composition overlapping that of intermediate plagioclase grains occurring in the breccia matrix, and inside the microgranophyre patches (Fig. 2). Similar to relationships observed in matrix surrounding the microgranophyre patches, feldspathic material associated with fracture networks in plagioclase grains can extend beyond the fractured host grain into adjacent fractured areas of matrix.

In the 12013,161 chip samples, FE-SEM imaging and EDS element mapping of matrix regions containing interpenetrating feldspathic material uncovered a number of

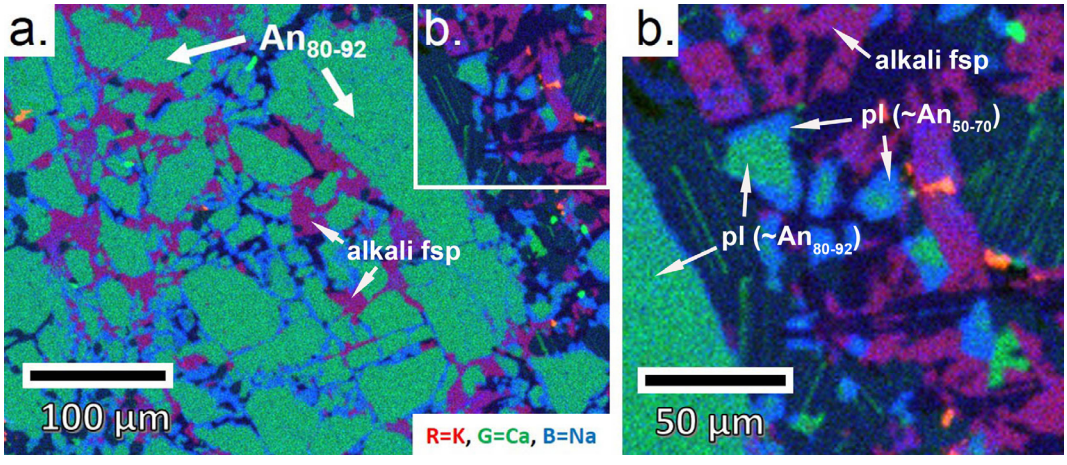

Fig. 13. Analytical FE-SEM EDS false color RGB composite K, Ca and Na element map of fracture network in breccia matrix plagioclase from sample 12013,167 (a, b). RGB 8-bit color channels have R = K counts, G = Ca counts, and B = Na counts. Scaling of B = Na channel is slightly enhanced to show distribution of intermediate plagioclase (blue) compositions relative to alkali feldspar (red) and more calcic plagioclase (green). Inset (b) shows detail of adjacent matrix containing small (5–10 μm) calcic plagioclase grains (green) with rims/overgrowths of intermediate-composition plagioclase (blue). (For interpretation of the references to colour in this figure legend, the reader is referred to the web version of this article.)

feldspathic mineral intergrowths with overall characteristics similar to the 12013,141 plagioclase/K-feldspar intergrowth. EDS composite K-Ca-Na element maps showing examples of two of these intergrowths are shown in Fig. 14. In these and other similar intergrowths, a key characteristic that is similar to the 12013,141 plagioclase/K-feldspar is the tendency for the more calcic plagioclase to occur as grain cores mantled or rimmed by more sodic, intermediate plagioclase, together with enclosed domains of K-feldspar.

7. DISCUSSION

7.1. Petrogenetic origins and ages of felsic rocks on the Moon

Recent studies utilizing remote sensing data report compelling evidence for relatively abundant sometimes large silicic non-mare volcanism on the Moon (Lawrence et al., 1998, 2003; Chevrel et al., 1999; Hagerty et al., 2006; Glotch et al., 2010; Jolliff et al., 2011; Wilson et al., 2015). On Earth, silicic (or felsic) magmatic centers are some of the largest volcanic landforms. These centers are multi-vent long-lived complexes found atop mantle-derived hotspots or related to extensional tectonic settings in grabens and marginal basins of continents. The primary eruptive products that characterize rhyolite volcanoes are large explosive ignimbrites and relatively small-volume rhyolite lavas and domes (e.g., Long Valley Caldera, USA). Underpinning these centers are typically long-lived, incrementally emplaced granitoid intrusions (Coleman et al., 2016). The silicic magmatic centers are periodically replenished by mantle-derived mafic magmas that produce silicic melt by partial crustal melting, crustal assimilation-fractional crystallization differentiation (AFC), or a combination of both (DePaolo, 1981; Davies et al., 1994; Simon et al., 2007, 2014).

To first order, understanding the generation of evolved lunar lithologies can be understood from basic petrological and geochemical principles, i.e., phase equilibria leading to a typical feldspathic mineralogy and element melt-mineral partitioning leading to incompatible element enrichment—including volatile species. It is difficult to distinguish whether the heating required to produce these melts was purely due to endothermic heating (i.e., radiogenic) or whether there are felsic clast materials in the Apollo collection that come from solidified silicic magma bodies that were produced by impact events, i.e., decompression-induced partial melting of crust (Hagerty et al., 2006; Johnson et al., 2018). Additionally, impact processes may metamorphose felsic precursor materials, as discussed herein.

Except for a few studies (e.g., Ryder, 1976), conventional terrestrial models of rhyolitic melt generation by processes of fractional crystallization and/or partial melting have not been called upon to explain the silicic lithologies returned by the Apollo astronauts. For decades silica liquid immiscibility (SLI), where a single chemically evolved melt separates into two co-existing melts (silica-rich and Fe-rich) has been the primary mechanism invoked (Hess et al., 1975; Rutherford et al., 1976; Warner et al., 1978; Taylor et al., 1980; Neal and Taylor, 1989). Although evidence for SLI has been found for some lunar samples (e.g., Jolliff et al., 1999), it is not an efficient method to generate silicic melt, (see Petford, 1996) and, therefore, has difficulty explaining the wide-spread and relatively large silicic surface features observed (Hagerty et al., 2006). This is because the magma distilling process must reflect extensive crystallization, which makes silicic melt segregation and extraction

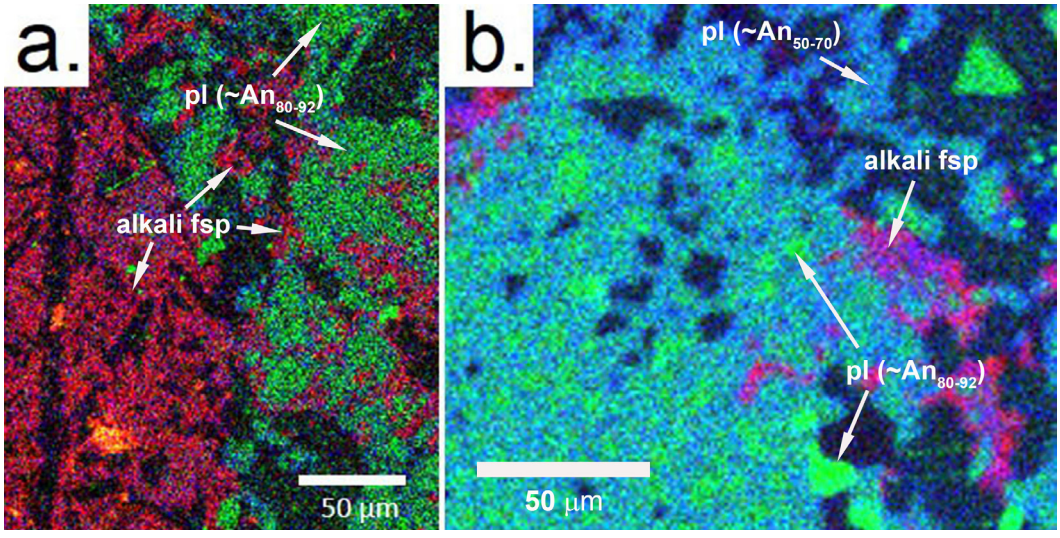

Fig. 14. Analytical FE-SEM EDS false color RGB composite K, Ca and Na element map of plagioclase + K-feldpar intergrowths in 12013,167 breccia matrix, adjacent to microgranophyre patches (a, b). RGB 8-bit color channels have R = K counts, G = Ca counts, and B = Na counts. Scaling of B = Na channel is slightly enhanced to show distribution of intermediate plagioclase (blue) compositions relative to alkali feldspar (red) and more calcic plagioclase (green). (For interpretation of the references to colour in this figure legend, the reader is referred to the web version of this article.)

physically difficult (Marsh, 2002). Moreover, little or no evidence has been seen of the required volumes of the associated Fe-rich melts nor can SLI explain why felsic lunar clasts (or surface features) have high Th and U; during SLI these and high field strength elements would be significantly partitioned into the Fe-rich mafic melt, not into the silica-rich melts (Gullikson et al., 2016).

Lunar felsites reported in the literature can be broken into two groups based on their Rare Earth Element (REE) abundance patterns: older ≥4.2 Ga samples that exhibit elevated trace element abundances, i.e., KREEP-like, and less KREEPy materials with characteristic "V"-shaped patterns derived from younger ~4.0 Ga magma(s) (Ryder, 1976; Warren et al., 1983; Marvin et al., 1991; Ryder and Martinez, 1991). Many lunar felsites contain petrographic and chemical features that are consistent with magmatic histories despite experiencing shock metamorphism to varying degrees. These include the ~4.32 Ga felsic materials from 12013 (Quick et al., 1981, recently dated by Thiessen et al., 2018) and a clast from 12032,366–19 recently reported by Seddio et al. (2013). Warren et al. (1983) concluded that both ~4.31 Ga 14303,209 (Shih et al., 1993; Meyer et al., 1996; Nemchin et al., 2008) and ~4.03 Ga 14321,1062 (Shih et al., 1993; Shih et al., 1994; Meyer et al., 1996; Simon et al., 2011) felsic clasts, before brecciation, were part of medium-grained intrusions (~1–2 mm, coarse by lunar standards). Likewise, Ryder (1976) showed that the lithic fragment population: coarse-grained granite, KREEP-rich quart-monzodiorite, and KREEP basalt in ~4.28 Ga (Meyer et al., 1996) 15405 were produced by plutonic differentiation and/or eruption of a KREEP basalt magma.

It should be noted that all of the studied materials appear to be older than the common "Late Heavy Bombardment" age of ~3.9 Ga measured in many lunar rocks (Turner et al., 1973; Tera et al., 1974). Secondary ion mass spectrometry measurements by Grange et al. (2013), Nemchin et al. (2017), Thiessen et al. (2018), and Bellucci et al. (2019) in these breccias indicate significant disturbance of the U-Pb isotope system and homogenization of Pb among accessory and major mineral phases, presumably by ≤3.9 Ga impact processes. These later resetting events that in some cases appear to be much younger (~1.9 Ga and 1.4 Ga) have heated materials in the studied breccia samples. It is expected that the population of older materials, e.g., clasts contained in 15405, should have experienced more impact reprocessing than the materials contained in the younger samples, e.g., clasts in 12013 and 14321, although locally the effects could vary. The impact history of the Moon (and Earth-Moon system) remains an ongoing field of study (see Cohen et al., 2000).

Silicic lunar surface features exhibit a crater count age range from 4.07 to 3.38 Ga. Hansteen Alpha, the largest of the silicic domes, is composed of several distinct units with surfaces emplaced between ~3.74 Ga and 3.5 Ga (Boyce et al., 2017). The Gruithuisen Delta and Gamma domes are slightly older, with ages of ~3.8 Ga. The Compton-Belkovich Complex (CBC) was active around the same time as the Mairan Domes, with the earliest possible onset of volcanism at ~3.8 Ga (Shirley et al., 2016). The extrusion of the Lassell Massif, the oldest of the lunar silicic domes, occurred between 3.95 Ga and 4.07 Ga (Ashley et al., 2016). It is notable, therefore, that nearly all isotopically dated felsites are significantly older than the crater count dated silicic surface features (Simon, 2018). Given the apparent age differences, it is unlikely that the silicic features observed on the lunar surface are the source regions for the silicic lithologies contained in the Apollo collection. Rather, the samples likely represent more ancient lithologies that have been destroyed or obscured by younger events, complicating our ability to study their petrogenetic origins.

7.2. Magmatic water estimates

An increasing number of sample-based studies have reported magmatic water contents from lunar materials (see review by McCubbin et al., 2015). In fact, volatile measurements in apatite contained in felsic samples (14303,205; 14321,1047; and 15404,51 ,55), which might be cogenetic with two of the clast samples studied herein (14321,1062 and 15405,78), have been made previously. Apatite grains in all of these ancient intrusive rocks indicate low magmatic water contents (<0.04 wt%) (Barnes et al., 2014; Robinson et al., 2016; and references therein). Notably, the inferred magmatic water contents based solely on OH^- measured in lunar apatite have been shown to be unreliable due to the co-dependent compatibilities of F, Cl, and OH^- (Boyce et al., 2014). Additionally, even when other volatile species are measured and site occupancy can be properly assessed, as is typical of current apatite studies, evolved magmas with high Cl/F can crystallize apatite that generally excludes OH^-, regardless of the water content of the magma (McCubbin et al., 2011; Boyce et al., 2014). This might explain the much higher estimates (~1 wt.%) reported by Mills et al. (2017) for felsic clasts in 15405. Alternatively, the difference between the apatite and feldspar water measurements from different samples may be real and related, at least in part, to the diverse mixture and/or history of materials in 15405, a complex lunar breccia.

Following the approach of Mills et al. (2017), the volatile distribution coefficients (D) between feldspar and host melts, and the H abundances measured in lunar feldspar can be used to estimate the magmatic water contents of the studied felsic clast materials. Accounting for corrections to FTIR absorption coefficients (when necessary) compiled literature D values range from ~0.001 to 0.004 for alkali-rich to calcium-rich feldspar, respectively (see Mosenfelder et al., 2015 and references therein). In addition to providing a frame of reference for the lunar feldspar measurements, our measurements of the terrestrial volcanic feldspar (Bishop Tuff, Long Valley, USA) can be used to refine existing estimates of volatile distribution between alkali feldspar and their host melts (Johnson and Rossman, 2004). The Bishop Tuff sanidines measured come from the Late Bishop Tuff sample LV51 in which quartz hosted melt inclusions have been measured previously and exhibit average H_2O contents of 2.9 ± 0.4 wt.% (2σ) and CO_2 of 140 ± 80 ppm (2σ) (Schmitt and Simon, 2004). Combining the feldspar and melt volatile abundances yields D_{H_2O} and D_{CO_2} values of $0.0011^{+0.0002}_{-0.0002}$ and $0.010^{+0.017}_{-0.004}$, respectively.

At face value the measured H contents in the lunar feldspar imply a significant range of magmatic water contents, from ~0.08–1.68 wt.% H_2O, and the measured felsite clasts nearly span this entire range from ~0.17–1.68 wt.% H_2O (see Table 3). Estimates of magmatic water contents involve assumptions of closed system behavior (i.e., no degassing or addition) and the use of appropriate distribution coefficients. If generation of the lunar melts followed standard melt differentiation processes one might expect their volatile abundances to generally correlate positively with other incompatible trace element abundances (i.e., KREEP). The plots of H-in-feldspar (and estimated H_2O melt) versus K_2O/CaO of the clasts in Fig. 15a and b prove inconsistent with this expectation. In fact, among the felsite materials the inverse relationship is observed, possibly implying water may have progressively degassed with increasing differentiation. The varying magmatic water estimates also appear to drop significantly over time (Simon et al., 2017). Such a temporal planetary-scale degassing history would be remarkable and could be tested by additional volatile-focused felsic clasts studies in which their crystallization ages and later heating events were also accurately dated. Next, we discuss micro-textural evidence that can be used to address petrogenetically which of the aforementioned models and/or assumptions are valid and that were used to support our preferred interpretations.

7.3. Felsite assemblages: Contrasting water abundances, formation histories, and the role of impacts

The expanding studies on volatile evolution in lunar magmatic systems have all applied a variety of sample characterization techniques to place measured volatile contents into context with the formation conditions (e.g., temperature, crystallization sequence) of the host samples (e.g., Saal et al., 2008; McCubbin et al., 2010; Hauri et al., 2011). In adopting this same approach, we have added the novel use of FIB-supported FE-STEM observations of defect substructures and compositional variations at the sub-micrometer to nanometer scale. Integrating the FE-STEM data with our other sample characterization results supports our ability to interpret: (1) whether a given volatile measurement corresponds to a phase occurring *in-situ* with other co-crystallized phases (as opposed to being an isolated single-grain clast), (2) the nature of the parent material for the co-crystallized assemblage (wholly molten, partially molten, or with some role for solid-state recrystallization), and (3) if occurring from a wholly or partially molten parent, whether crystallization occurred within a larger volcanic- or intrusive-scale magmatic system, or on a much smaller local scale, as might occur in shock melting due to impact. Finally, a key additional evaluation is the extent to which post-crystallization, overprinting effects from shock (or other thermal events) may have substantially modified a melt-derived assemblage, including its volatile content.

For the 15405 microgranophyre assemblage whose volatile content was measured by Mills et al. (2017), our FE-STEM observations have confirmed that the feldspathic portion of this assemblage, which in all probability was initially crystalline, is amorphous. Amorphization probably occurred by some combination of direct shock amorphization/melting, or heating likely associated with shock. The tridymite coexisting with the glass may have been part of

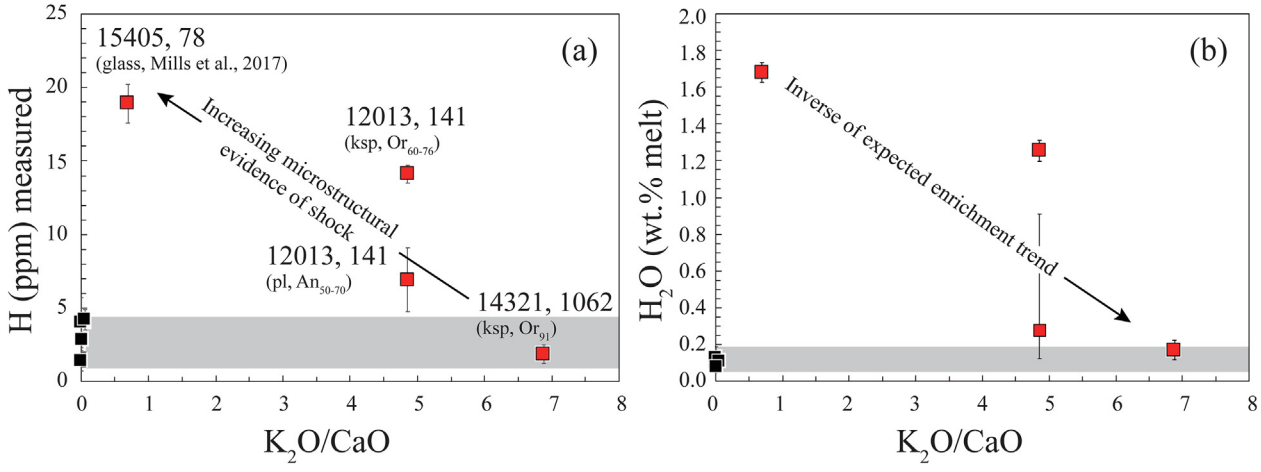

Fig. 15. Hydrogen-in-feldspar measurements (a) and estimated magmatic water contents (b) compared to K_2O/CaO in felsic (red symbols) and mafic (black symbols) samples. Secondary ion microprobe data for two FAN samples from Hui et al. (2017) included with the mafic samples measured herein. K_2O and CaO data from Haskin et al. (1974); Wänke et al. (1975); Quick et al. (1977); Ryder (1976); Warren and Wasson (1980); Warren et al. (1983). Hydrogen abundances (and estimated H_2O wt.% melt values) are means with their associated 2 SD uncertainties. The H_2O wt.% melt estimated from 12013 plagioclase (pl) is the exception in which the larger uncertainties reflect propagation of the range of reported volatile distribution coefficients (Hamada et al., 2013; Mosenfelder and Hirschmann, 2016; this study). H measurements of alkali feldspar (ksp) from 12013 granophyre material and pl from adjacent 12013 "plagioclase + alkali feldspar" material are distinct (see text). Composition of the ksp intergrown with the An_{50-70} plagioclase is ~Or_{50}. Bulk felsite K_2O/CaO of 12013 clast material reported by Quick et al. likely represents averaging among these distinct more local melt compositions (i.e., granophyre material and plagioclase + alkali feldspar material, the latter of which appears to represent a mixture between assimilated xenocrysts and a more felsic melt). (For interpretation of the references to colour in this figure legend, the reader is referred to the web version of this article.)

the original crystalline microgranophyre assemblage, but evidence at the FE-STEM image scale suggests that it more likely transformed from quartz in the solid-state or directly crystallized from the melt at temperatures in excess of the quartz-tridymite transition at ~860 °C (Heaney, 1994). From the peak temperature the assemblage attained, it evidently cooled slowly enough to undergo open-system cation exchange resulting in a significant net loss of alkalis (or alternatively gain of Si + Al). It is unclear whether during this open system behavior other volatiles would have been driven out of the feldspar (suggesting it initially had a higher H content), or if H was added from the local enclosing breccia matrix. The matrix may have acquired volatiles from a more extended wet reservoir that possibly got that way from addition of near surface volatiles (Kayama et al., 2018; Stopar et al., 2018).

The microstructure, phase assemblage, and H content (Mills et al., 2017) of the glassy microgranophyre stands out in contrast to the 14321 and 12013 felsites, whose feldspars both have lower H contents, are wholly crystalline, occur with a lower-temperature silica phase (quartz) and have minimal solid-state shock effects based on FE-STEM observations (e.g., Figs. 3 and 4). Although the H contents of the 14321 and 12013 crystalline feldspars are both significantly lower than the 15405 glassy feldspathic assemblages, it is notable that they are still measurably different from one another. The 14321 K-feldspars have H contents that fall in the same range as mafic assemblage feldspars measured here and in previous studies (Hui et al., 2017; Mosenfelder et al., 2017). The 12013 feldspars have higher H concentrations, both in the plagioclase/K-feldspar intergrowth and the microgranophyre, which establishes them as some of the highest H content crystalline lunar feldspars so far reported (Fig. 15). In addition, in 12013 the H contents for feldspars in the two adjacent, contrasting, host assemblages, are also measurably different.

The coordinated sample characterization that we have performed on the 14321 and 12013 samples, together with the results of previous studies, suggests that despite sharing attributes that point to a melt-derived origin, the host assemblages for the feldspars we have studied from these samples are very different in their microstructures, modal mineralogies, and feldspar compositions on a range of scales. These differences in turn argue for substantially different origins for the parent melts, the environment of crystallization of those melts, and potentially provide a way to account for the different H contents of the constituent feldspars.

For the 14321 felsite clasts, our FE-SEM and EPMA results align with previous studies in finding consistent chemical homogeneity in the near end-member K-feldspars, which occur with quartz in a relatively simple bimodal assemblage containing no other feldspar compositions and few other phases. Although similar to the nomenclature used by Warren et al. (1983), we have added the prefix "micro" to our descriptions of the 14321 granophyric texture, the sizes of the individual grains, at consistently just below 1 mm, are nevertheless much coarser than the vast majority of lunar felsites (the 14303 felsite clasts also described by Warren et al., 1983, being one possible exception). By comparison the patchy microgranophyre in 12013, with an order of magnitude smaller grain size, is more truly "micro".

Our characterization of the well-known 14321 felsite clasts, and their constituent feldspars, are in line with previous work, and provide few options to diverge from the baseline interpretation that the 14321 clasts likely sample a volumetrically significant unit of relatively homogeneous, moderately fine-grained, granitic igneous rock (i.e., a magma body as opposed to a localized partial melt). Moreover, to previous studies we have added FE-STEM results showing that, although the 14321 rock fragments ended up being disaggregated and dispersed in an impact melt breccia, the feldspars in these fragments, whose volatile content we have measured, survived the breccia formation event without significant degrees of shock metamorphism that may have altered their intrinsic volatile contents. With final regard to recent suggestions that the parent igneous unit for the 14321 felsite may be from Earth and partially exchanged with lunar chemical reservoirs near the time it formed ~4.0 Ga, i.e., homogenizing the Pb isotope signatures in feldspar (Bellucci et al., 2019), our mineral and textural findings do not support nor rule out these claims. However, it is noteworthy that the H content of feldspar and quartz in this sample is lower than any terrestrial felsic rock. In fact, the H abundance in 14321,1062 quartz is lower than any natural SiO_2-phase ever reported. Additionally, clast material from this granite lithology exhibits perhaps the most robust crystallization age of any lunar material (e.g., concordant Sm-Nd, Rb-Sr, K-Ca mineral isochron and U-Pb zircon crystallization ages, Shih et al., 1985, 1993; Bogard et al., 1994; Meyer et al., 1996; Simon et al., 2011).

Felsite in 12013 has significant differences in microstructures and compositions compared to the 14321 clasts, and suggests an origin related to impact effects from the breccia formation process itself. Suggestions that a significant fraction of the felsite material in 12013 was derived from a felsic precursor assemblage that underwent whole or partial impact melting when the parent breccia was formed appear surprisingly early in the initial studies on 12013 (Drake et al., 1970, Albee et al., 1970, Quick et al., 1981). All of these proposals were based on a key observation that, although made with earlier-generation analytical tools, matches what we have reported here in greater detail: the intimate interpenetration of the 12013 microgranophyre felsite assemblage within the intergranular spaces of the host breccia matrix. These observations include the report by Drake et al. (1970) of felsite assemblages forming veinlets in fractured mineral grains that also match one of our findings.

The earlier studies all arrived at slightly different versions of an explanation in which a parent melt, partial melt, or "fluid" of granitic composition infiltrated the host breccia's intergranular spaces in response to an impact event that most likely melted (or mechanically fluidized) a pre-existing felsite assemblage during the breccia formation process (Albee et al., 1970, Drake et al., 1970, Quick et al., 1981). The compositional and microstructural details obtained in this study, which greatly expand on what was

possible in the earlier work, have ended up supporting the general tenets of this early explanation, and have not pointed strongly towards petrogenetic alternatives. In line with earlier work, we have documented multiple, pervasive examples of felsic material distributed in fractures or intergranular void space that connect with microgranophyre patches in a reservoir-conduit-type arrangement. We have also documented, in greater detail than previous studies, that the microgranophyre patches themselves contain a disequilibrium assemblage of calcic and intermediate composition plagioclase occurring with alkali feldspar that is compositionally heterogeneous at the micrometer scale along a well-defined Ca + Na enrichment trend. These relations are consistent with crystallization of an impact-derived melt in which sub-mm scale compositional heterogeneity occurred because of small scale variations in the fused fraction of different shock-melted phases (in this case primarily different feldspars). The limited and localized scale of shock melting would be expected to produce melt patches that would cool relatively quickly because of the thermal heterogeneities intrinsic to clast-rich, partially melted impact breccias. The net result would be insufficient time to homogenize a compositionally heterogeneous shock melt that was either not hot enough, or slowly cooled enough, to finish digesting grains of plagioclase that it had incorporated as xenocryts from the breccia matrix. The fact that the microgranophyre patches contain relic un-melted plagioclase, but not relic K-feldspar or silica preserved from what was likely a felsic target material may explain the apparent eutectic preference for shock melting these phases compared to plagioclase.

When taken as a whole, the microstructural and compositional relationships described by current and previous studies of 12013 microgranophyre patches clearly do not reflect crystallization within an intrusive felsic melt body of any appreciable size. The possibility that the microgranophyre patches are simply shock-deformed clasts that retain a primary assemblage from a larger igneous unit is inconsistent with multiple lines of evidence, including our FE-STEM imaging results showing no appreciable solid-state shock effects in the constituent quartz and feldspar assemblage.

In an additional expansion on previous work, we have learned more about the mineralogical details, melt-solid reactions and re-crystallization effects relating to the conduit-like distribution of felsic material throughout the intergranular spaces of the host breccia matrix assemblage. In and around the felsic assemblages occurring inside fracture spaces and intergranular voids in the breccia matrix we have found multiple examples of melt-solid reactions between matrix grains of calcic plagioclase and the interpenetrating melt phase. As previously described and shown in Figs. 13 and 14, the reactions are typified by the formation of intermediate-composition plagioclase as a reaction product between felsic melt that contacts or surrounds grains of more calcic plagioclase. In the most common and less complex example, the reaction produces simple rim-type overgrowths of intermediate plagioclase around single grain cores of calcic plagioclase. Other more complex examples, however, include the plagioclase/K-feldspar intergrowth in which we measured H contents of ~7 ppm and ~14 ppm, respectively. This intergrowth shows evidence of having formed when a relatively fine-grained aggregate of calcic plagioclase grains reacted with interpenetrating melt containing K and Na, and re-crystallized to a three-phase feldspar assemblage made up of relic grain cores of calcic plagioclase enclosed in an assemblage of intermediate, plagioclase and minor K-feldspar.

Given the evidence that a distributed, interpenetrating, impact-generated silicate melt drove the melt-solid recrystallization that formed the plagioclase/K-feldspar intergrowth, we consider it likely that interaction with this melt affected the H content of the plagioclase. Of greater interest, however, is the direction of the effect: The plagioclase/K-feldspar assemblage in 12013, shows substantial re-crystallization effects directly caused by interaction with impact-generated melt, and the plagioclase inside it has a measurably higher H content than K-feldspar from the 14321 microgranophyre. The latter assemblage, although making up clasts enclosed in crystallized impact melt, shows no evidence of impact-generated recrystallization, and retains a microstructure and mineral composition characteristic of crystallization inside a volumetrically significant unit of relatively homogeneous granitic magma. Our preferred interpretation, therefore, is that the higher H content of the 12013 plagioclase reflects interaction with an impact melt carrying significant volatiles, available for transfer to any grains the melt substantially interacted with or directly caused to crystallized. The latter case would apply to the K-feldspar from the 12013,141 microgranophyre assemblage, which also show evidence of an elevated H content compared to the 14321 feldspar, but crystallized directly from the distributed, impact-generated melt, as opposed to simply interacting with it through a melt-solid reaction.

8. CASE FOR A SIGNIFICANTLY DRY/DEGASSED MOON LOCALLY HYDRATED BY IMPACTS

Based on negative correlation between measured feldspar H contents and both K_2O/CaO ratios and extent of shock microstructures in the studied felsites, a case can be made that their volatiles do not simply reflect incompatible element enrichment of an indigenous source. It is possible that all of the felsites originally had higher intrinsic/magmatic water contents and that the low to background level H abundance measured in 14321,1062 is in line with extensively degassed volcanic rocks on Earth (e.g., Moussallam et al., 2014). In fact, degassing would likely be enhanced at the low pressure conditions at the surface of the Moon. It should be noted, however, that many evolved volcanic rocks that have experienced degassing contain minerals and melt inclusions that retain a record of their magmatic volatile contents (e.g., Westrich et al., 1988; Hervig et al., 1989; Schmitt, 2001; Schmitt and Simon, 2004; this study). More to the point, the water content indicative of most granitic rocks from Earth show that magmatic degassing is much more limited. Although it is not totally clear how

the felsite material in 12013,141 originated, the clast material studied in 14321,1062 and 15405,78 come from plutonic sources, rather than volcanic extrusions (Quick et al., 1981; Warren et al., 1983).

The measured water contents in the studied materials may also not represent their primary signatures because most of the lunar surface has been heating to some degree from impact events (e.g., Grange et al., 2013). However, we suggest that because 14321,1062 reflects the sample studied with the least amount of shock modification, whereas the "water-rich" felsites 12013 and 15405 exhibit significantly more shock features, the water measurements more likely reflect volatile addition to the disturbed felsites rather than water removed from the more pristine one. It is worth noting that with further clast investigations we might find that this preliminary water content-shock level correlation is oversimplified, and that other felsic magmas on the Moon have different histories and water contents. There might be some "wet" felsic magmas based on the timing, location, and source of the magmas. Nevertheless, if the measured volatiles represent magmatic abundances, it remains an open question as to why the older felsites contain no volatile-bearing silicate phases and why the youngest, most evolved felsite, with little shock metamorphism and minimal isotopic disturbance (e.g., well-behaved concordant isochron ages) is extremely water-poor (Fig. 15a and b).

McCubbin et al. (2015) coupled mass balance calculations with the partitioning behavior of volatiles between LMO melts and nominally anhydrous minerals to demonstrate how various volatile species could be fractionated during LMO crystallization. They showed how evolution

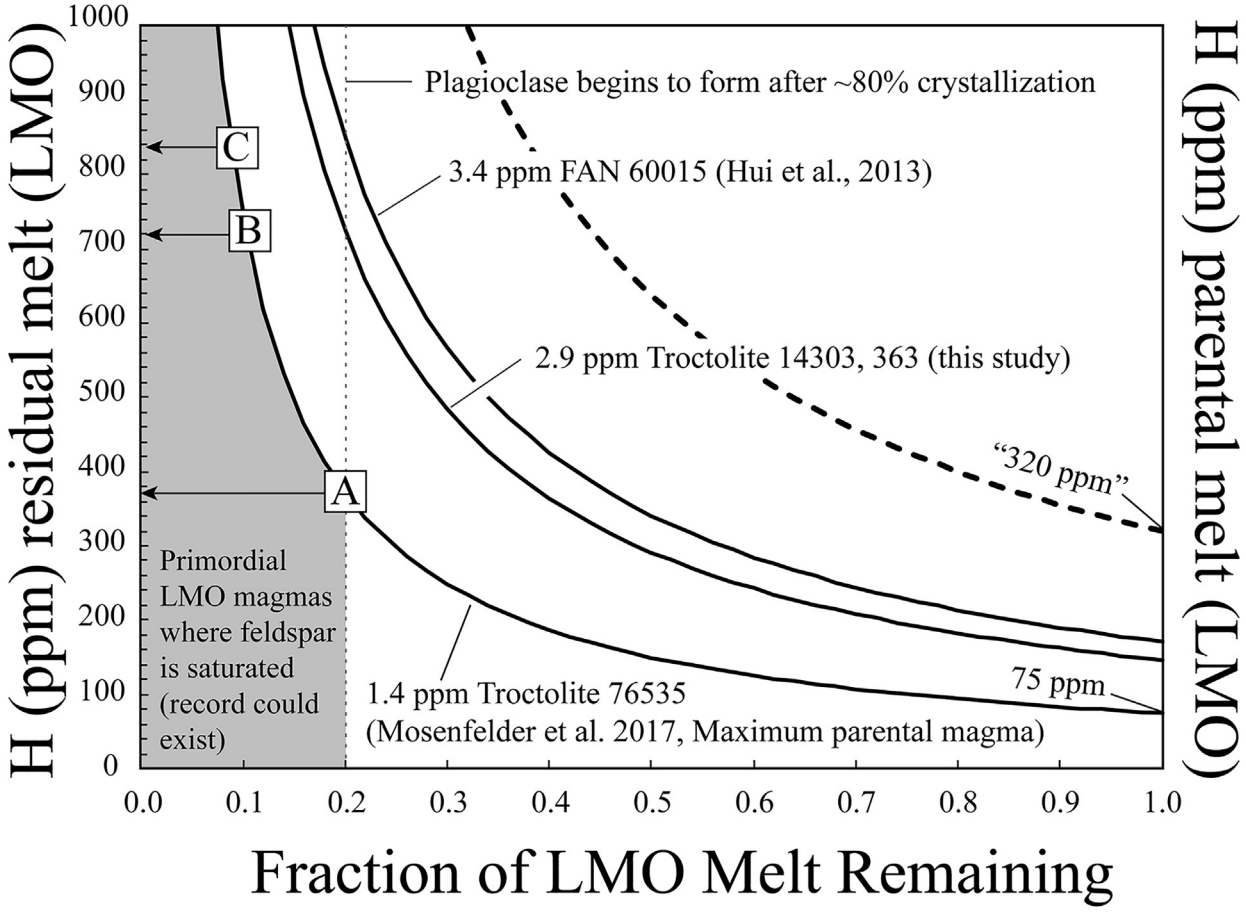

Fig. 16. Diagram showing Rayleigh fractionation model curves used to place constraints on parental magma water composition of LMO based on feldspar H measurements of primordial materials (FANs and troctolites). Curves derived from residual melt compositions computed assuming a H melt-plagioclase distribution coefficient of 0.004 (Hamada et al., 2013). Dashed curve indicates the original model of Hui et al. (2013) for FAN 60015. The reported parental magma H abundance drops from ~320 ppm to ~170 ppm after corrections (Mosenfelder et al., 2017) have been applied to their FTIR data. Points A-C indicate possible melt H abundances and degree of differentiation of primordial melts based on feldspar measurements for FAN 60015 and troctolites 14303, 363 and 76535, assuming an initial LMO value of 75 ppm computed from the lowest H measurement reported (1.4 ppm for plagioclase in 76535). Samples with lower H values potentially recording an even lower parental magma H of the LMO may exist, but will not be observed until lower H detection limits are routinely achieved. Model curves assume constant time integrated distribution coefficients for olivine and pyroxene prior to plagioclase saturation at 80% crystallization of parental magma ($F > 0.2$). The 'wet' melts and high bulk silicate Moon estimated by Hui et al. were likely also overestimated because of the unrealistic assumption that the feldspars measured were the "first" to form from the lunar magma ocean.

of the LMO would produce reservoirs with heterogeneous distributions of volatiles and how later mantle dynamics (i.e., overturn and melting) could further localize mantle volatile sources. Some such process is needed to explain the heterogeneous distributions of magmatic volatiles in the lunar materials, namely those derived from the relatively dry or degassed ancient highlands (and secondary crustal lithologies in this study) as compared to the relatively hydrated mantle source regions invoked to explain picritic glasses and mare basalts (Saal et al., 2008; Hauri et al., 2011; McCubbin et al., 2011; Robinson and Taylor, 2014; Robinson et al., 2016). Finally, it is unclear how effective volatile addition via impacts might be into the deeper parts of the interior of the Moon. Perhaps, crust-breaching impacts, i.e., Barnes et al. (2016a,b), could transport water into the interior producing heterogeneously distributed volatile reservoirs in the lunar mantle while at the same time degas the crust?

Based on the microtextural observations described above, it appears that the volatiles in 12013 and 15405 felsite clasts were exogenous to the Moon and added directly through the impact of "hydrous" asteroidal and/or cometary bodies (Greenwood et al., 2011; Svetsov and Shuvalov, 2015; Barnes et al., 2016a,b; Daly and Schultz, 2018; Tartèse and Anand, 2013) or indirectly by impact-induced water-rock reactions on the lunar surface (Kayama et al., 2018; Stopar et al., 2018). These impacts would have either produced the felsites through large scale melting of lunar rocks and hydrous bolides followed by fractional crystallization of these melt mixtures or partial melting and mixing of hydrous impactors with preexisting evolved materials. In both cases, the negligibly elevated 14321,1062 magmatic water content that is similar to or just slightly higher than that computed for the more mafic materials studied herein (Fig. 15b) likely reflects enrichment of the endogenous volatiles of an appreciably dry or previously degassed lunar interior. It is possible that the dry 14321,1062 felsite represents degassing due to impact heating at the lunar surface that escaped further rehydration by younger impact processes. If true, then this degassing must have been a localized phenomenon because the water contents of the older 12013 and 15405 clasts must have escaped significant degassing as their water contents imply Earth-like wet granitic magmas.

A dry or previously degassed source locally hydrated by impact can explain the felsites and is consistent with the evidence for low water abundances among the range of ancient magnesian suite, alkali suite, KREEP-rich, FANs, and troctolitic lithologies, e.g., Sharp et al. (2010), Hui et al. (2013, 2017), Barnes et al. (2014, 2016a,b), Boyce et al. (2015), Robinson et al. (2016), and Mosenfelder et al. (2017). This preferred interpretation does not support a 'wet' magma ocean → urKREEP scenario (Hui et al., 2013). However, corrections to the H contents of the materials studied by Hui et al. 2013 (see Mosenfelder et al., 2015) and more realistic assumptions related to the percent crystallization shown in Fig. 16 demonstrate that the water abundance in the parental magma (i.e., initial LMO) required to explain the measurements (100′s ppm) reported by Hui et al. (2013) is overestimated.

9. CONCLUSIONS

The Moon accreted dry or degassed early. Lunar felsic material, with its high concentrations of incompatible elements, should have some of the highest concentrations of hydrogen on the Moon. However, results herein suggest felsic magmas on the Moon were quite dry. The 'wet' felsic magmas tentatively ascribed to felsite clast materials in Apollo samples 12013 and 15405 likely obtained little water from the lunar interior, but rather incorporated volatiles during impact of volatile-bearing bolides locally at the surface of the Moon. The extremely dry felsite material in 14321,1062, given its relatively low amount of microstructural evidence for shock metamorphism, gives the best estimate for the water content (~0.2 wt.% H_2O) of the felsic endmember of differentiation of the bulk Moon. Future missions that sample silicic dome materials would allow us to resolve whether lunar felsic magmatism is primarily impact generated and how much water occurs in these potential surface reservoirs. At the same time, targeting silicic volcanism for sample return would help to resolve the apparent age paradox between the isotopically dated felsic samples and crater-counting dated silicic features distributed over relatively wide areas of the lunar surface.

Declaration of Competing Interest

The authors declare that they have no known competing financial interests or personal relationships that could have appeared to influence the work reported in this paper.

ACKNOWLEDGEMENTS

Analysis of the rare lunar felsite materials studied herein would not have been possible without the Apollo era scientists, NASA engineers, and astronauts. NASA curation staff are thanked for their commitment to maintain the integrity of the samples and the skillful processing. Apollo Sample Curator Ryan Zeigler and members of CAPTEM are thanked for sample allocations. Discussions and NanoSIMS analytical advancements with Eric Hauri at DTM were critical to the success of this work and he will be sorely missed. This contribution benefited from the work of three anonymous reviewers, and the editorial handling of Dr. Alex Nemchim. This work was supported by NASA Planetary Science Division and Solar System Workings Program, United States Government to JIS and RC.

APPENDIX A. SUPPLEMENTARY MATERIAL

Supplementary data to this article can be found online at https://doi.org/10.1016/j.gca.2020.02.008.

REFERENCES

Adams J. B., Anders E., Dence M. R., Haskin L. A., Head III J. W., Hubbard N. J., McCord T. B., Nyquist L. E., Reed G. W., Tatsumoto M., Walker R. M., and Wood J. A. (1976) Interdisciplinary studies by the Imbrium Consortium, Vol. 1, pp. 152.

Albarede F. (2009) Volatile accretion history of the terrestrial planets and dynamic implications. *Nature* **461**, 1227–1233.

Albee A. L., Burnett D. S., Chodos A. A., Haines E. L., Huneke J. C., Papanastassiou D. A., Podosek F. A., Russ, III, G. P. and Wasserburg G. J. (1970) Mineralogic and isotopic investigations on lunar rock 12013. *Earth Planet. Sci. Lett.* **9**, 137–163.

Ashley J., Robinson M. S., Stopar J. D., Glotch T. D., Hawke B. R., van der Bogert C. H. and Hiesinger H. (2016) The Lassell Massif—a silicic lunar volcano. *Icarus* **273**, 248–261.

Barnes J. J., Kring D. A., Tartese R., Franchi I. A., Anand M. and Russell S. S. (2016a) An asteroidal origin for water in the Moon. *Nat. Commun.* **7**. Article #11684.

Barnes J. J., Tartèse R., Anand M., McCubbin F. M., Franchi I. A., Starkey N. A. and Russell S. S. (2014) The origin of water in the primitive Moon as revealed by the lunar highlands samples. *Earth Planet. Sci. Lett.* **390**, 244–252.

Barnes J. J., Tartese R., Anand M., McCubbin F. M., Neal C. R. and Franchi I. A. (2016b) Early degassing of lunar urKREEP by crust-breaching impact(s). *Earth Planet. Sci. Lett.* **447**, 84–94.

Bellucci J. J., Nemchin A. A., Grange M., Robinson K. L., Collins G., Whitehouse M. J., Snape J. F., Norman M. D. and Kring D. A. (2019) Terrestrial-like zircon in a clast from an Apollo 14 breccia. *Earth Planet. Sci. Lett.* **510**, 173–185.

Berger E. L. and Keller L. P. (2015) A hybrid ultramicrotomy-FIB technique for preparing serial electron transparent thin sections from particulate samples. *Microscopy Today*, 18–22.

Bhattacharya R. S., Saran S., Dagar A., Chauhan P., Chauhan M. and Ajai K. (2013) Endogenic water on the Moon associated with non-mare silicic volcanism: implications for hydrated lunar interior. *Curr. Sci.* **105**, 685–691.

Boctor N. Z., Alexander C. M. O. D., Wang J. and Hauri E. (2003) The sources of water in Martian meteorites: clues from hydrogen isotopes. *Geochim. Cosmochim. Acta* **67**, 3971–3989.

Bogard D. D., Garrison D. H., Shih C. Y. and Nyquist L. E. (1994) 39Ar- 40Ar dating of two lunar granites: The age of Copernicus. *Geochim. Cosmochim. Acta* **58**, 3093–3100.

Boyce J. M., Giguere T. A., Hawke B. R., Mouginis-Mark P. J., Robinson M. S., Lawrence S. J., Trang D. and Clegg-Watkins C. (2017) Hansteen Mons: An LROC geological perspective. *Icarus* **283**, 254–267.

Boyce J. W., Liu Y., Rossman G. R., Guan Y., Eiler J. M., Stolper E. M. and Taylor L. A. (2010) Lunar apatite with terrestrial volatile abundances. *Nature* **466**, 466–469.

Boyce J. W., Tomlinson S. M., McCubbin F. M., Greenwood J. P. and Trieman A. H. (2014) The Lunar Apatite Paradox. *Science* **344**, 400–402.

Boyce J. W., Trieman A. H., Guan Y., Ma C., Eiler J. M., Gross J., Greenwood J. P. and Stolper E. M. (2015) The chlorine isotope fingerprint of the lunar magma ocean. *Sci. Adv.* **1**, e1500380.

Chevrel S. D., Pinet P. C. and Head J. W. (1999) Gruithuisen domes region: A candidate for an extended nonmare volcanism unit on the Moon. *J. Geophys. Res.* **104**, 16515–16530.

Coleman D. S., Mills R. D. and Zimmerer M. J. (2016) The pace of plutonism. *Elements* **12**, 97–102.

Cohen B. A., Swindle T. D. and Kring D. A. (2000) Support for the lunar cataclysm hypothesis from lunar meteorite impact melt ages. *Science* **290**, 1754–1756.

Daly R. T. and Schultz P. H. (2018) The delivery of water by impacts from planetary accretion to present. *Sci. Adv.* **4**, 1–11.

Davies G. R., Halliday A. N., Mahood G. A. and Hall C. M. (1994) Isotopic constraints on the production rates, crystallisation histories and residence times of pre-caldera silicic magmas, Long Valley, California. *Earth Planet. Sci. Lett.* **125**, 17–37.

DePaolo D. J. (1981) Trace element and isotopic effects of combined wallrock assimilation and fractional crystallization. *Earth Planet. Sci. Lett.* **53**, 189–202.

Drake M. J., McCallum I. S., McKay G. A. and Weill D. F. (1970) Mineralogy and petrology of Apollo 12 sample no. 12013: A progress report. *Earth Planet. Sci. Lett.* **9**, 103–123.

Glotch T. D., Lucey P. G., Bandfield J. L., Greenhagen B. T., Thomas I. R., Elphic R. C., Bowles N. E., Wyatt M. B., Allen C. C., Donaldson Hanna K. L. and Paige D. A. (2010) Highly silicic compositions on the Moon. *Science* **329**, 1510–1513.

Grange M. L., Pidgeon R. T., Nemchin A. A., Timms N. E. and Meyer C. (2013) Interpreting U-Pb data from primary and secondary features in lunar zircon. *Geochimica et Cosmochimica Acta* **101**, 112–132.

Greenwood J. P., Itoh S., Sakamoto N., Warren P., Taylor L. A. and Yurimoto H. (2011) Hydrogen isotope ratios in lunar rocks indicate delivery of cometary water to the Moon. *Nat. Geosci.* **4**, 79–82.

Gullikson A. L., Hagerty J. J., Reid M. R., Rapp J. F. and Draper D. S. (2016) Silicic lunar volcanism: Testing the crustal melting model. *Am. Min.* **101**, 2312–2321.

Hagerty J. J., Lawrence D. J., Hawke B. R., Vaniman D. T., Elphic R. C. and Feldman W. C. (2006) Refined thorium abundances for lunar red spots: Implications for evolved, nonmare volcanism on the Moon. *J. Geophys. Res* **111**(E06002).

Hamada M., Ushioda M., Fujii T. and Takahashi E. (2013) Hydrogen concentration in plagioclase as a hygrometer of arc basaltic melts: Approaches from melt inclusion analyses and hydrous melting experiments. *Earth Planet. Sci. Lett.* **365**, 253–262.

Han J., Keller L. P., Lui M.-C., Needham A. W., Hertwig A. T., Messenger S. and Simon J. I. (2020) A coordinated microstructural and isotopic studie of a Wark-Lovering rim on a Vigarano CAI. *Geochim. Cosmochim. Acta* **269**, 639–660.

Haskin L. A., Shih C.-Y., Bansal B. M., Rhodes J. M., Wiesmann H. and Nyquist L. E. (1974) Chemical evidence for the origin of 76535 as a cumulate. *Lunar Planet. Sci. Conf. Proc.* **5**, 1213–1225.

Hauri E., Wang J., Dixon J. E., King P. L., Mandeville K. C. and Newman S. (2002) SIMS analysis of volatiles in volcanic glasses, 1 Calibration, matrix effects and comparison with FTIR. *Chem. Geol.* **183**, 99–114.

Hauri E., Shaw A., Wang J., Dixon J., King P. and Mandeville C. (2006a) Matrix effects in hydrogen isotope analysis of silicate glasses by SIMS. *Chem. Geol.* **235**, 352–365.

Hauri E. H., Gaetani G. A. and Green T. H. (2006b) Partitioning of water during melting of the Earth's upper mantle at H2O-undersaturated conditions. *Earth Planet. Sci. Lett.* **248**, 715–734.

Hauri E. H., Saal A. E., Rutherford M. C. and Van Orman J. A. (2015) Water in the Moon's interior: Truth and consequences. *Earth Planet. Sci. Lett.* **409**, 252–264.

Hauri E. H., Weinreich T., Saal A. E., Rutherford M. C. and Van Orman J. A. (2011) High pre-eruptive water contents preserved in lunar melt inclusions. *Science* **333**, 213–215.

Heaney P. J. (1994) Structure and chemistry of the low-pressure silica polymorphs. In *Silica: Physical Behavior, Geochemistry and Materials Applications* (eds. P. J. Heaney, C. T. Prewitt and G. V. Gibbs). Mineralogical Society of America, Washington, D. C., pp. 1–40.

Hervig R., Nelia D., Westrich H. R. and Kyle P. R. (1989) Preeruptive water content of rhyolitic magmas as determined by ion microprobe analyses of melt inclusions in phenocrysts. *J. Volcanol. Geoth. Res.* **36**, 293–302.

Hess P. C., Rutherford M. J., Guillemette R. N., Ryerson F. J. and Tuchfeld H. A. (1975) Residual products of fractional crystallization of lunar magmas - an experimental study. *Lunar Planet. Sci. Conf. Proc.* **6**, 895–909.

Hui H., Guan Y., Chen Y., Peslier A. H., Zhang Y., Liu Y., Flemming R. L., Rossman G. R., Eiler J. M., Neal C. R. and Osinski G. R. (2017) A heterogeneous lunar interior for hydrogen isotopes as revealed by the lunar highland samples. *Earth Planet. Sci. Lett.* **473**, 14–23.

Hui H., Peslier A. H., Zhang Y. and Neal C. R. (2013) Water in lunar anorthosites and evidence for a wet early Moon. *Nat. Geosci.* **6**, 177–180.

Johnson E. A. (2006) Water in nominally anhydrous crustal minerals: Speciation, concentration, and geologic significance. *Water in nominally anhydrous minerals*, 2006, 62, 117–154.

Johnson E. A. and Rossman G. R. (2003) The concentration and speciation of hydrogen in feldspars using FTIR and 1H MAS NMR spectroscopy. *Am. Min.* **88**, 901–911.

Johnson E. A. and Rossman G. R. (2004) A survey of hydrous species and concentrations in igneous feldspar. *Am. Min.* **89**, 560–600.

Johnson T. E., Gardiner N. J., Miljkovic K., Spencer C. J., Kirkland C. L., Bland P. A. and Smithies H. (2018) An impact melt origin for Earth's oldest known evolved rocks. *Nat. Geosci.* **11**, 798–799.

Jolliff B. L., Floss C., McCallum I. S. and Schwartz J. M. (1999) Geochemistry, petrology, and cooling history of 14161, 7373: A plutonic lunar sample with textural evidence of granitic-fraction separation by silicate-liquid immiscibility. *Am. Min.* **84**, 821–837.

Jolliff B. L., Gillis J. J., Haskin L. A., Korotev R. L. and Wieczorek M. A. (2000) Major lunar crustal terranes: Surface expressions and crust-mantle origins. *J. Geophys. Res* **105**, 4197–4216.

Jolliff B. L., Wiseman S. A., Lawrence S. J., Tan T. N., Robinson M. S., Sato H., Hawke B. R., Scholten F., Oberst J., Hiesinger H., van der Bogert C. H., Greenhagen B. T., Glotch T. D. and Paige D. A. (2011) Non-mare silicic volcanism on the lunar farside of Compton-Belkovich. *Nat. Geosci.* **4**, 556–571.

Joy K. H., Zolensky M. E., Nagashima K., Huss G. R., Ross D. K. and McKay D. S. (2012) Direct detection of projectile relics from the end of the lunar basin-forming epoch. *Science* **336**, 1426–1429.

Kayama M., Tomioka N., Ohtani E., Seto Y., Nagaoka H., Gotze J., Miyake A., Ozawa S., Sekine T., Miyahara M., Tomeoka K., Matsumoto M., Shoda N., Hirao N. and Kobayashi T. (2018) Discovery of moganite in a lunar meteorite as a trace of H_2O ice in the Moon's regolth. *Sci. Adv.* **4**, eaar4378.

Klima R., Cahill J., Hagerty J. and Lawrence D. (2013) Remote detection of magmatic water in Bullialdus Crater on the Moon. *Nat. Geosci.* **6**, 737–741.

Koga K., Hauri E., Hirschmann M. and Bell D. (2003) Hydrogen concentration analyses using SIMS and FTIR: Comparison and calibration for nominally anhydrous minerals. *Geochem. Geophys. Geosyst.* **4**(2), 1019. https://doi.org/10.1029/2002GC000378.

Kronenberg A. K., Yund R. A. and Rossman G. R. (1996) Stationary and mobile hydrogen defects in potassium feldspar. *Geochim. Cosmochim. Acta* **60**, 4075–4094.

Lally J. S., Fischer R. M., Christie J. M., Griggs D. T., Heuer A. H., Nord G. L. and Radcliffe S. V. (1972) Electron petrography of Apollo 14 and 15 rocks. In *Proceedings of the 3rd Lunar Science Conference*, pp. 401–422.

Lawrence D. J., Elphic R. C., Feldman W. C., Prettyman T., Gasnualt O. and Maurice S. (2003) Small area thorium features on the lunar surface. *J. Geophys. Res.* **108**(E9).

Lawrence D. J., Feldman W. C., Barraclough B. L., Binder A. B., Elphic R. C., Maurice S. and Thomsen D. R. (1998) Global elemental maps of the Moon: The Lunar Prospector gamma-ray spectrometer. *Science* **281**, 1484–1489.

Lindstrom M. M., Marvin U. B., Vetter S. K. and Shervais J. W. (1988) Apennine front revisited: diversity of Apollo 15 highland rock types. In *Proceedings of the 18th Lunar and Planetary Science Conference*, pp. 169–185.

Marsh B. D. (2002) On bimodal differentiation by solidification front instability in basaltic magmas, part 1: basic mechanics. *Geochim. Cosmochim. Acta* **66**, 2211–2229.

Marvin U. B., Holmberg B. B., Lindstrom M. M. and Martinez R. R. (1991) New observations on the quartz monzodiorite-granite suite. *Lunar Planet. Sci. Conf. Proc.* **21**, 119–135.

McConnell J. D. C. (1965) Electron optical study of effects associated with partial inversion in a silicate phase. *Phil. Mag.* **11**, 1289–1301.

McConnell J. D. C. (1971) Electron-optical study of phase transformation. *Mineral. Mag.* **38**, 1–20.

McCubbin F. M., Jolliff B. L., Nekvasil H., Carpenter P. K., Zeigler R. A., Steele A., Elardo S. M. and Lindsley D. H. (2011) Fluorine and chlorine abundances in lunar apatite: Implications for heterogeneous distributions of magmatic volatiles in the lunar interior. *Geochim. Cosmochim. Acta* **75**, 5073–5093.

McCubbin F. M., Steele A., Hauri E. H., Nekvasil H., Yamashita N. and Hemley R. J. (2010) Nominally hydrous magmatism on the Moon. *PNAS* **27**, 11223–11228.

McCubbin F. M., Vander Kaaden K. E., Tartese R., Klima R. L., Liu Y., Mortimer J., Barnes J. J., Shearer C. K., Treiman A. H., Lawrence D. J., Elardo S. M., Hurley D. M., Boyce J. W. and Anand M. (2015) Magmatic volatiles (H, C, N, F, S, Cl) in the lunar mantle, crust, and regolith: Abundances, distributions, processes, and reservoirs. *Am. Min.* **100**, 1668–1707.

Meyer C. (2016) The lunar sample compendium. *Astromaterials Research & Exploration Science (ARES)*, https://curator.jsc.nasa.gov.

Meyer C., Williams I. S. and Compston W. (1996) Uranium-lead ages for lunar zircons: Evidence for a prolonged period of granophyre formation from 4.32 to 3.88 Ga. *Meteorit. Planet. Sci.* **31**, 370–387.

Meyer C. and Yang S. V. (1988) Tungsten-bearing yttrobetafite in lunar granophyre. *Am. Min.* **73**, 1420–1425.

Milliken R. E. and Li S. (2017) Remote detection of widespread indigenous water in lunar pyroclastic deposits. *Nat. Geosci.* **10**, 561–565.

Mills R. D., Simon J. I., Alexander C. M. O. D., Wang J. and Hauri E. H. (2017) Water in alkali feldspar: The effect of rhyolite generation on the lunar hydrogen budget. *Geochem. Perspect. Lett.* **3**, 115–123.

Mosenfelder J. L., Caseres J. R. and Hirschmann M. M. (2017) A comprehensive SIMS study of hydrogen, fluorine, and chlorine in nominally anhydrous minerals from 15 lunar samples. *48th Lunar and Planetary Science Conference, Abst. #2473*.

Mosenfelder, J.L. and Hirschmann, M.M. (2016) SIMS Measurements of Hydrogen and Fluorine in Lunar Nominally Anhydrous Minerals, 47th Lunar and Planetary Science Conference. LPI, The Woodlands, Texas, p. Abst. # 1903.

Mosenfelder J. L., Rossman G. R. and Johnson E. A. (2015) Hydrous species in feldspars: A reassessment based on FTIR and SIMS. *Am. Min.* **100**, 1209–1221.

Moussallam Y., Oppenheimer C., Scaillet B., Gaillard F., Kyle P., Peters N., Hartley M., Berlo K. and Donovan A. (2014) Tracking the changing oxidation state of Erebus magmas, from mantle to surface, driven by magma ascent and degassing. *Earth Planet. Sci. Lett.* **393**, 200–209.

Neal C. R. and Taylor L. A. (1989) The nature and barium partitioning between immiscible melts - A comparison of experimental and natural systems with reference to lunar granite petrogenesis. *Lunar Planet. Sci. Conf. Proc.* **19**, 209–218.

Nemchin A. A., Jeon H., Bellucci J. J., Timms N. E., Snape J. F., Kilburn M. R. and Whitehouse M. J. (2017) Pb-Pb ages of feldspathic clasts in two Apollo 14 breccia samples. *Geochimica et Cosmochimica Acta* **217**, 441–461.

Nemchin A. A., Pidgeon R. T., Whitehouse M. J., Vaughan J. P. and Meyer C. (2008) SIMS U-Pb study of zircon from Apollo 14 and 17 breccias: implications for evolution of lunar KREEP. *Geochim. Cosmochim. Acta* **72**, 668–689.

Petford N. (1996) Dykes and diapirs? *Trans. Royal Soc. Edinburgh* **87**, 105–114.

Petro N. E., Isaacson P. J., Pieters C. M., Jolliff B. L., Carter L. M. and Klima R. L. (2013) Presence of OH/H20 associated with the lunar Compton-Belkovich volcanic complex identified by the moon mineralogy mapper (M^3). *44th Lunar and Planetary Science Conference, Abst. #2688*.

Quick J. E., Albee A. L., Ma M.-S., Murali A. V. and Schmitt R. A. (1977) Chemical compositions and possible immiscibility of two silicate melts in 12013. *Lunar Planet. Sci. Conf. Proc.* **8**, 2153–2189.

Quick J. E., James O. B. and Albee A. L. (1981) Petrology and petrogenesis of lunar breccias 12013. In *Proceedings of the 12th Lunar Science Conference*, pp. 117–172.

Righter K., Abell P., Agresti D., Berger E. L., Burton A. S., Delaney J. S., Fries M. D., Gison E. K., Haba M. K., Harrington R., Herzog G. F., Keller L. P., Locke D., Lindsay F. N., McCoy T. J., Morris R. V., Nagao K., Nakamura-Messenger K., Niles P. B., Nyquist L. E., Park J., Peng Z. X., Shih C.-Y., Simon J. I., Swisher, III, C. C., Tappa M. J., Turrin B. D. and Zeigler R. A. (2015) Mineralogy, petrology, chronology, and exposure history of the Chelyabinsk meteorite and parent body. *Meteorit. Planet. Sci.* **59**, 1790–1819.

Roedder E. and Weiblen P. W. (1970) Lunar petrology of silicate melt inclusions, Apollo 11 rocks. *Proceedings of the Apollo 11 Lunar Science Conference, Geochim. Cosmochim. Acta* **801**, Supplement 1.

Robinson K. L. and Taylor G. J. (2014) Heterogeneous distribution of water in the Moon. *Nat. Geosci.* **7**, 401–408.

Robinson K. L., Barnes J. J., Hagashima K., Thomen A., Franchi I. A., Huss G. R., Anand M. and Taylor G. J. (2016) Water in evolved lunar rocks: Evidence for multiple reservoirs. *Geochim. Cosmochim. Acta* **188**, 244–260.

Rutherford M. J., Hess P. C., Ryerson F. J., Campbell H. W. and Dick P. A. (1976) The chemistry, origin and petrogenetic implications of lunar granite and monzonite. *Lunar Planet. Sci. Conf. Proc.* **7**, 1723–1740.

Ryder G. (1976) Lunar sample 15405 - Remnant of a KREEP basalt-granite differentiated pluton. *Earth Planet. Sci. Lett.* **29**, 255–268.

Ryder G., Stoeser D. B., Marvin U. B. and Bower J. F. (1975) Lunar granites with unique ternary feldspars. *Lunar Planet. Sci. Conf. Proc.* **6**, 435–449.

Ryder G. and Martinez R. R. (1991) Evolved hypabyssal rocks from Station 7, Apennine Front, Apollo 15. *Lunar Planet. Sci. Conf. Proc.* **21**, 137–150.

Saal A. E., Hauri E. H., Cascio M. L., Van Orman J. A., Rutherford M. C. and Cooper R. F. (2008) Volatile content of lunar volcanic glasses and the presence of water in the Moon's interior. *Nature* **454**, 192–195.

Schmitt A. K. (2001) Gas-saturated crystallization and degassing in large-volume, crystal-rich dacitic magmas from the Altiplano-Puna, northern Chile. *J. Geophys. Res.* **106**, 30561–30578.

Schmitt A. K. and Simon J. I. (2004) Boron isotopic variations in hydrous rhyolitic melts: a case study from Long Valley, California. *Contrib. Miner. Petrol.* **146**, 590–605.

Seddio S. M., Jolliff B. L., Korotev R. L. and Zeigler R. A. (2013) Petrology and geochemistry of lunar granite 12032,366–19 and implications for lunar granite petrogenesis. *Am. Min.* **98**, 1697–1713.

Seddio S. M., Korotev R. L., Jolliff B. L. and Wang A. (2015) Silica polymorphs in lunar granite: Implications for granite petrogenesis on the Moon. *Am. Min.* **100**, 1533–1543.

Sharp Z. D., Shearer C. K., McKeegan K. D., Barnes J. D. and Wang Y. Q. (2010) The chlorine isotope composition of the Moon and implications for an anhydrous mantle. *Science* **329**, 1050–1053.

Shih C. Y., Nyquist L. E., Bogard D. D. and Wiesmann H. (1994) K-Ca and Rb-Sr dating of two lunar granites: Relative chronometer resetting. *Geochim. Cosmochim. Acta* **58**, 3101–3116.

Shih C. Y., Nyquist L. E. and Wiesmann H. (1993) K-Ca chronology of lunar granites. *Geochim. Cosmochim. Acta* **57**, 4827–4841.

Shih C.-Y., Nyquist L. E., Bogard D. D., Wooden J. L., Bansal B. M. and Wiesmann H. (1985) Chronology and petrogenesis of a 1.8 g lunar granite clast: 14321, 1062. *Geochim. Cosmochim. Acta* **49**, 411–426.

Shirley K. A., Zanetti M., Jolliff B., van der Bogert C. H. and Hiesinger H. (2016) Crater-size-frequency distribution measurements and age of the Compton-Belkovich volcanic complex. *Icarus* **273**, 214–223.

Simon J. I. (2018) Age paradox of silicic lithologies and remotely observed surface features on the Moon. In New Views of the Moon 2-Asia, Abst. #2070.

Simon J. I., Christoffersen R., Wang J., Alexander C. M. O. D., Mills R. D. and Hauri E. H. (2017) Low to extremely low water abundances measured in nominally anhydrous minerals in mafic to granitic apollo rock clasts. *48th Lunar and Planetary Science Conference, Abst. #1248*.

Simon J. I., Reid M. R. and Young E. D. (2007) Lead isotopes by LA-MC-ICPMS: Tracking the emergence of mantle signatures in an evolving silicic magma system. *Geochim. Cosmochim. Acta* **71**, 2014–2035.

Simon J. I., Renne P. R. and Mundil R. (2008) Implications of pre-eruptive magmatic histories of zircons for U-Pb geochronology of silicic extrusions. *Earth Planet. Sci. Lett.* **266**, 182–194.

Simon J. I., Shih C. Y. and Nyquist L. E. (2011) K-Ca and Rb-Sr dating of lunar granite 14321 revisited. *42nd Lunar and Planetary Science Conference, Abst. #2754*.

Simon J. I., Weis D., DePaolo D. J., Renne P. R., Mundil R. and Schmitt A. K. (2014) Assimilation of preexisting Pleistocene intrusions at Long Valley by periodic magma recharge accelerates rhyolite generation: rethinking the remelting model. *Contrib. Miner. Petrol.* **167**, 1–34.

Simonds C. H., Phinney W. C., Warner J. L., McGee P. E., Geeslin J., Brown R. W. and Rhodes J. M. (1977) Apollo 14 revisited, or breccias aren't so bad after all. *Lunar Planet. Sci. Conf. Proc.* **8**, 1869–1893.

Stoeser D. B., Marvin U. B., Wood J. A., Wolfe R. W. and Bower J. F. (1974) Petrology of a stratified boulder from South Massif, Taurus-Littrow. *Lunar Planet. Sci. Conf. Proc.* **5**, 355–377.

Stopar J. D., Jolliff B. L., Speyerer E., Asphaug E. and Robinson M. S. (2018) Potential impact-induced water-solid reactions on the Moon. *Planet. Space Sci.* **162**, 157–169.

Svetsov V. V. and Shuvalov V. V. (2015) Water delivery to the Moon by asteroidal and cometary impacts. *Planet. Space Sci.* **117**, 444–452.

Tartèse R. and Anand M. (2013) Late delivery of chondritic hydrogen into the lunar mantle: insights from mare basalts. *Earth Planet. Sci. Lett.* **361**, 480–486.

Tartese R., Anand M., McCubbin F. M., Elardo S. M., Shearer C. K. and Franchi I. A. (2014) Apatites in lunar KREEP basalts: The missing link to understanding the H isotope systematics of the Moon. *Geology* **42**, 363–366.

Taylor G. J., Warner R. D., Keil K., Ma M.-S. and Schmitt R. A. (1980) Silicate liquid immiscibility, evolved lunar rocks and the formation of KREEP. In *Proceedings of the Conference on the Lunar Highlands Crust*, pp. 339–352.

Tera F., Papanastassiou D. A. and Wasserburg G. J. (1974) Isotopic evidence for a terminal lunar cataclysm. *Earth Planet. Sci. Lett.* **22**, 1–21.

Thiessen F., Nemchin A. A., Snape J. F., Bellucci J. J. and Whitehouse M. J. (2018) Apollo 12 breccia 12013: Impact-induced partial Pb loss in zircon and its implications for lunar geochronology. *Geochim. Cosmochim. Acta* **230**, 94–111.

Turner G., Cadogan P. H. and Yonge C. J. (1973) Argon selenochronology. *Proceedings of the fourth Lunar Science Conference* **2**, 1889–1914.

Usui T., Alexander C. M. O., Wang J., Simon J. I. and Jones J. H. (2012) Origin of water and mantle-crust interactions on Mars inferred from hydrogen isotopes and volatile elements abundances of olivine-hosted melt inclusions of primitive shergottites. *Earth Planet. Sci. Lett.* **410**, 140–151.

Usui T., Alexander C. M. O., Wang J., Simon J. I. and Jones J. H. (2015) Meteoritic evidence for a previously unrecognized hydrogen reservoir on Mars. *Earth Planet. Sci. Lett.* **357–358**, 119–129.

Wänke H., Palme H., Baddenhausen H., Dreibus G., Jagoutz E., Kruse H., Palme C., Spettel B., Teschke F. and Thacker R. (1975) New data on the chemistry of lunar samples - Primary matter in the lunar highlands and the bulk composition of the moon. *Lunar Planet. Sci. Conf. Proc.* **6**, 1313–1340.

Warner R. D., Taylor G. J., Mansker W. L. and Keil K. (1978) Clast assemblages of possible deep-seated (77517) and immiscible-melt (77538) origins in Apollo 17 breccias. *Lunar Planet. Sci. Conf. Proc.* **9**, 941–958.

Warren P. H., Taylor G. J., Keil K., Shirley D. N. and Wasson J. T. (1983) Petrology and chemistry of two "large" granite clasts from the Moon. *Earth Planet. Sci. Lett.* **64**, 175–185.

Warren P. H. and Wasson J. T. (1980) Further foraging for pristine nonmare rocks - Correlations between geochemistry and longitude. *Lunar Planet. Sci. Conf. Proc.* **11**, 431–470.

Westrich H. R., Stockman H. W. and Eichelberger J. C. (1988) Degassing of rhyolitic magma during ascent and emplacement. *J. Geophys. Res.* **93**, 6503–6511.

Wilson J. T., Eke V. R., Massey R. J., Elphic R. C., Jolliff B. L., Lawrence D. J., Llewellin E. W., McElwaine J. N. and Teodoro L. F. A. (2015) Evidence for explosive silicic volcanism on the Moon from the extended distribution of thorium near the Compton-Belkovich Volcanic Complex. *J. Geophys. Res. Planets* **120**, 92–108.

Associate editor: Alexander Nemchin

Update

Geochimica et Cosmochimica Acta
Volume 288, Issue , 1 November 2020, Page 389–394

DOI: https://doi.org/10.1016/j.gca.2020.08.001

Available online at www.sciencedirect.com

ScienceDirect

Geochimica et Cosmochimica Acta 288 (2020) 389–394

Geochimica et Cosmochimica Acta

www.elsevier.com/locate/gca

Corrigendum

Corrigendum to "Volatiles in lunar felsite clasts: Impact-related delivery of hydrous material to an ancient dry lunar crust" [Geochim. Cosmochim. Acta 276 (2020) 299–326]

J.I. Simon — Center for Isotope Cosmochemistry and Geochronology, Astromaterials Research and Exploration Science, NASA Johnson Space Center, Houston, TX 77058, USA

R. Christoffersen — Center for Isotope Cosmochemistry and Geochronology, Astromaterials Research and Exploration Science, NASA Johnson Space Center, Houston, TX 77058, USA

J. Wang — Department of Terrestrial Magnetism, Carnegie Institution of Washington, Washington, DC 20015-1305, USA

M.D. Mouser [1] — Center for Isotope Cosmochemistry and Geochronology, Astromaterials Research and Exploration Science, NASA Johnson Space Center, Houston, TX 77058, USA

R.D. Mills — Department of Geological Sciences, University of North Carolina, Chapel Hill, NC 27599, USA

D.K. Ross — Center for Isotope Cosmochemistry and Geochronology, Astromaterials Research and Exploration Science, NASA Johnson Space Center, Houston, TX 77058, USA

Z. Rahman — Jacobs, NASA Johnson Space Center, Mail Code XI3, Houston, TX 77058, USA

DOI of original article: 10.1016/j.gca.2020.02.008.

https://doi.org/10.1016/j.gca.2020.08.001

C.M.O'D. Alexander Department of Terrestrial Magnetism, Carnegie Institution of Washington, Washington, DC 20015-1305, USA

Received 3 July 2020; revised 1 August 2020; accepted in revised form 3 August 2020

The reported *nomenclature* for hydrogen concentration in Tables 2 and 3 & Figs. 15 and 16 of Simon et al. (2020) has been modified for clarity.

Hydrous components were measured in nominally anhydrous minerals, primarily lunar feldspar, and reported by Simon et al. (2020). In the feldspar mineral structure, these components are contained in the form of OH, H_2O, and/or NH_4^+ molecules (Johnson, 2006 and references therein). The advantages of the ion microprobe technique employed by Simon et al. (2020) include high spatial resolution, apparent insensitivity to crystal orientation, high precision, and low detection limits, but unlike complementary spectroscopy techniques (i.e., FTIR) they preclude assignment of molecular species (Mosenfelder et al., 2015). Convention in the lunar sample community is to report major elemental abundances and hydrogen as oxides, H_2O is the oxide for H. This convention was not followed by Simon et al. (2020), but rather the measured hydrogen component was reported as H to avoid the appearance of assigning the measured hydrogen concentration to a specific molecular species. The speciation of the hydrous component in terrestrial feldspars varies predominantly between OH and H_2O, with no apparent correlation to feldspar composition, and only slight correlation to volcanic-to-plutonic igneous rock type (Johnson and Rossman, 2004).

Table 2
Volatile Abundances Measured in Secondary Standards by NanoSIMS.

Sample	C (ppm)	H (ppm)	H_2O (ppm)	F (ppm)	S (ppm)*	Cl (ppm)	Cl/F	Material	Magmatic H_2O (wt%)**
RY-79-17		9.3	83.3	0.42	0.04	0.00	0.01	Adularia	
RY-79-17	0.7	9.3	82.8	0.42	0.03	0.01	0.01	Adularia	
RY-79-17		9.7	86.9	0.42	0.44	0.20	0.49	Adularia	
RY-79-17	0.7	9.8	87.3	0.39	0.03	0.02	0.06	Adularia	
RY-79-17	0.6	9.1	81.0	0.42	0.03	0.00	0.01	Adularia	
RY-79-17		9.4	83.6	0.40	*32.86*	0.04	0.09	Adularia	
Average	**0.6**	**9.4**	**84.2**	**0.41**	**0.11**	**0.05**	**0.11**		
LV51	0.4	3.5	31.3	0.95	0.03	0.01	0.01	Sanidine	2.78
LV51	0.4	3.8	34.2	0.96	0.04	0.01	0.01	Sanidine	3.04
LV51	0.4	3.6	32.3	0.96	0.05	0.02	0.02	Sanidine	2.88
Average	**0.4**	**3.6**	**32.6**	**0.96**	**0.04**	**0.01**	**0.01**		
JSC std mount	0.0	0.2	2.1	0.10	0.02	1324	12,809	Suprasil (SiO_2)	
DTM std mount	0.2	0.2	1.7	0.08	0.02			Suprasil (SiO_2)	
JSC sample mount	0.2	0.1	0.9	0.11	0.02	1301	11,787	Suprasil (SiO_2)	
JSC sample mount	0.2	0.2	1.8	0.11	0.02	1265	11,069	Suprasil (SiO_2)	
JSC sample mount	0.2	0.2	1.5	0.12	0.02	1400	12,026	Suprasil (SiO_2)	
JSC sample mount	0.4	0.2	1.4	0.11	0.03	1298	11,913	Suprasil (SiO_2)	
DTM std mount	0.1	0.1	1.1	0.08	0.03	1603	20,555	Suprasil (SiO_2)	
Average	**0.2**	**0.2**	**1.5**	**0.10**	**0.02**	**1365**	**13,360**		

Measured hydrogen component represented as H and H_2O mass fractions for clarity.
* S variabiliy likely reflects contribution from mineral impurities.
** Computed magmatic H_2O content based on empirically derived distribution coefficient given by average H_2O of quartz bearing melt inclusions in LV51 (Schmitt and Simon, 2004).

[1] Current address: Department of Earth and Planetary Sciences, The University of Tennessee, Knoxville, TN 37996, USA.

Table 3
Volatile Abundances Measured in Lunar Mineral Phases by NanoSIMS.

Sample	C (ppm)	H (ppm)	H_2O (ppm)	F (ppm)	S (ppm)*	Cl (ppm)	Cl/F	Material	Magmatic H_2O (wt%)**
15405,255	0.6	0.5	4.5	0.85	0.03	0.01	0.01	Plagioclase	0.11
15405,255	0.8	0.5	4.3	0.84	0.08	0.06	0.07	Plagioclase	0.11
15405,255	2.1	0.6	5.4	0.74	0.03	0.01	0.02	Plagioclase	0.14
15405,255	1.1	0.4	3.8	0.87	0.04	0.03	0.04	Plagioclase	0.10
Average	**1.2**	**0.5**	**4.5**	**0.83**	**0.05**	**0.03**	**0.03**		**0.11**
14321,1062	0.5	0.2	2.0	0.38	3.19	2.26	6.01	Alkali-feldspar	0.20
14321,1062	0.4	0.2	1.8	0.60	0.03	0.02	0.03	Alkali-feldspar	0.18
14321,1062	0.4	0.2	1.9	0.41	0.03	0.06	0.14	Alkali-feldspar	0.19
14321,1062	1.4	0.3	2.5	0.58	0.08	0.04	0.07	Alkali-feldspar	0.25
14321,1062	0.4	0.2	1.9	1.32	0.06	0.30	0.22	Alkali-feldspar	0.19
14321,1062	0.8	0.2	1.6	0.58	0.03	0.02	0.04	Alkali-feldspar	0.16
14321,1062	0.7	0.2	1.5	1.00	2.96	3.27	3.26	Alkali-feldspar	0.15
14321,1062	0.7	0.2	1.5	1.05	11.85	4.67	4.46	Alkali-feldspar	0.15
14321,1062	0.8	0.2	2.1	0.58	0.03	0.05	0.09	Alkali-feldspar	0.21
Average	**0.7**	**0.2**	**1.9**	**0.72**	**2.03**	**1.19**	**1.59**		**0.19**
14321,1062	0.3	0.0	0.1	0.09	0.03	0.00	0.04	SiO_2	
14321,1062	0.6	0.0	0.3	0.10	0.02	0.06	0.61	SiO_2	
14321,1062	0.3	0.0	−0.1	0.12	0.02	0.00	0.02	SiO_2	
14321,1062	0.2	0.0	−0.2	0.11	0.03	0.00	0.04	SiO_2	
Average#	**0.3**	**0.0**	**0.0**	**0.10**	**0.02**	**0.02**	**0.18**		
15405,255	1.7	0.3	3.0	3.48	0.31	0.01	0.00	Clinopyroxene	
15405,255	1.8	0.4	3.6	3.91	0.70	0.01	0.00	Clinopyroxene	
15405,255	0.7	0.5	4.0	1.86	0.14	0.14	0.08	Orthopyroxene	
Average	**1.4**	**0.4**	**3.6**	**3.08**	**0.38**	**0.05**	**0.03**		
14303,363	0.6	0.4	3.5	1.35	0.19	0.61	0.45	Plagioclase	0.09
14303,363	0.7	0.3	2.7	1.73	0.06	1.61	0.93	Plagioclase	0.07
14303,363	0.6	0.3	2.4	1.10	0.37	1.54	1.40	Plagioclase	0.06
Average	**0.6**	**0.3**	**2.9**	**1.39**	**0.2**	**1.3**	**0.9**		**0.07**
14303,363	1.2	0.6	5.5	4.38	0.10	0.30	0.07	Orthopyroxene	
14303,363	1.3	0.7	5.9	3.68	2.09	0.13	0.03	Orthopyroxene	
14303,363	1.1	0.7	6.1	3.58	0.04	0.01	0.00	Orthopyroxene	
Average	**1.2**	**0.7**	**5.8**	**3.88**	**0.74**	**0.15**	**0.04**		
12013,141 Clast 11	0.6	0.8	6.7	0.13	0.08	0.11	0.87	Plagioclase	0.67
12013,141 Clast 11	0.5	0.7	5.9	0.76	0.04	0.45	0.59	Plagioclase	0.59
12013,141 Clast 11	0.5	0.9	8.1	0.14	0.09	0.14	1.01	Plagioclase	0.81
Average	**0.5**	**0.8**	**6.9**	**0.34**	**0.07**	**0.24**	**0.83**		**0.69**
12013,141 Clast 11	4.4	1.6	14.7	0.16	0.08	0.14	0.87	Alkali-feldspar	1.47
12013,141 Clast 11	3.8	1.5	13.5	0.18	0.09	0.08	0.46	Alkali-feldspar	1.35
Average^	**4.1**	**1.6**	**14.1**	**0.17**	**0.09**	**0.11**	**0.67**		**1.41**

Measured hydrogen component represented as H and H_2O mass fractions for clarity.
* S variability likely reflects contribution from mineral impurities.
** Computed range of magmatic H_2O content assuming $D = 0.001$ (evolved melt) and 0.004 (primitive melt), respectively.
# natural SiO_2 is used to define the baseline.
^ C is high in these alkali-feldspar analyses, SEM imagery shows no evidence that ion beam hit cracks or grain boundaries.

The use of this generic H "water content" has led to confusion and this corrigendum is intended to clarify this. The reported hydrogen abundances in Simon et al. (2020) in Tables 2 and 3, Figs. 15 and 16, and throughout the text are all the mass fraction of H_2O (ppm), not the mass fraction of H (ppm).

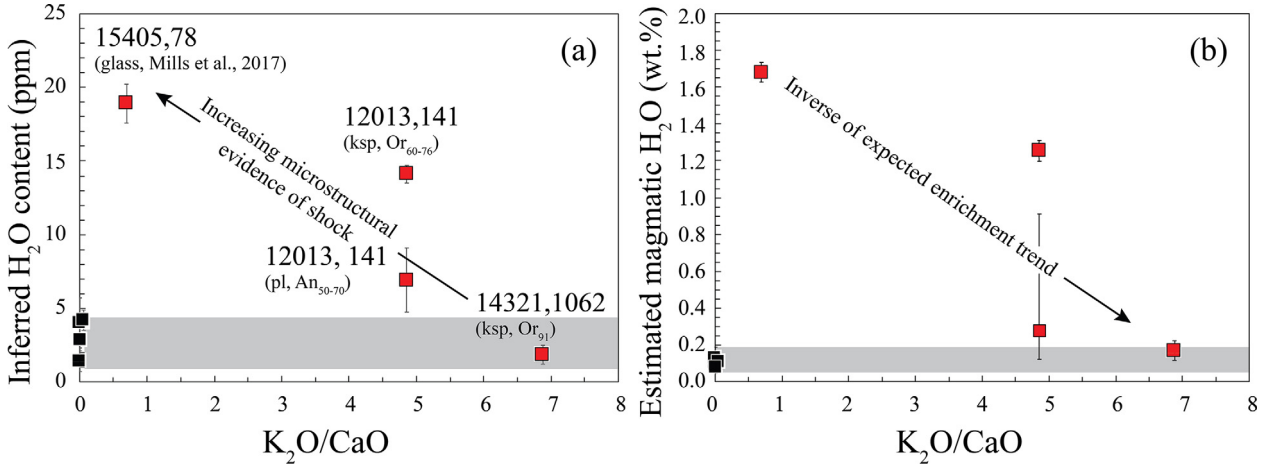

Fig. 15. (Modified after Fig. 15 in Simon et al., 2020). Inferred H_2O-in-feldspar based on secondary ion microprobe measurements (a) and estimated magmatic water contents (b) compared to K_2O/CaO in felsic (red symbols) and mafic (black symbols) samples. Secondary ion microprobe data for two FAN samples from Hui et al. (2017) included with the mafic samples measured herein. K_2O and CaO data from Haskin et al. (1974), Wänke et al. (1975), Quick et al. (1977), Ryder (1976), Warren and Wasson (1980) and Warren et al. (1983). Inferred H_2O-in-feldspar abundances (and estimated H_2O wt.% melt values) are means with their associated 2 SD uncertainties. The H_2O wt.% melt estimated from 12013 plagioclase (pl) is the exception in which the larger uncertainties reflect propagation of the range of reported volatile distribution coefficients (Hamada et al., 2013; Mosenfelder et al., 2016; Simon et al., 2020). The measurements used to infer H_2O in alkali feldspar (ksp) from 12013 granophyre material and plagioclase from adjacent 12013 "plagioclase + alkali feldspar" material are distinct (see Simon et al., 2020). Composition of the ksp intergrown with the An_{50-70} plagioclase is ~Or_{50}. Bulk felsite K_2O/CaO of 12013 clast material reported by Quick et al. likely represents averaging among these distinct more local melt compositions (i.e., granophyre material and plagioclase + alkali feldspar material, the latter of which appears to represent a mixture between assimilated xenocrysts and a more felsic melt).

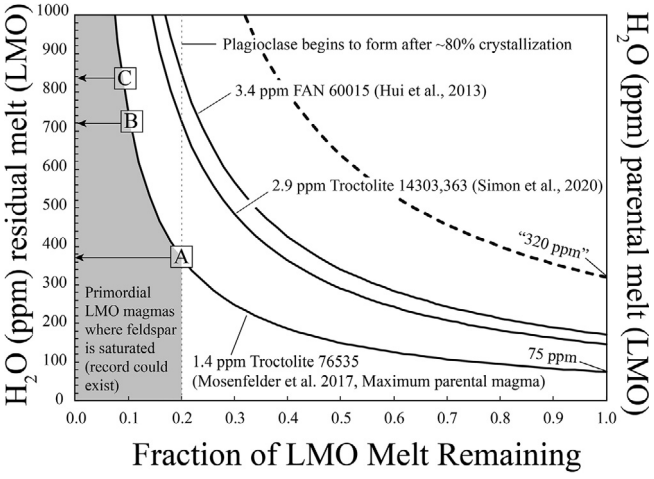

Fig. 16. (Modified after Fig. 16 in Simon et al., 2020). Diagram showing Rayleigh fractionation model curves used to place constraints on parental magma water composition of LMO based on inferred H_2O-in-feldspar contents of primordial materials (FANs and troctolites). Curves derived from residual melt compositions computed assuming a H_2O melt-plagioclase distribution coefficient of 0.004 (Hamada et al., 2013). Dashed curve indicates the original model of Hui et al. (2013) for FAN 60015. The reported parental magma H_2O abundance drops from ~320 ppm to ~170 ppm after corrections (Mosenfelder et al., 2017) have been applied to their FTIR data. Points A–C indicate possible melt H_2O abundances and degree of differentiation of primordial melts based on feldspar measurements for FAN 60015 and troctolites 14303, 363 and 76535, assuming an initial LMO value of 75 ppm computed from the lowest inferred H_2O-in-feldspar contents (1.4 ppm for plagioclase in 76535). Samples with lower inferred H_2O values potentially recording an even lower parental magma H_2O of the LMO may exist, but will not be observed until lower hydrogen component detection limits are routinely achieved. Model curves assume constant time integrated distribution coefficients for olivine and pyroxene prior to plagioclase saturation at 80% crystallization of parental magma ($F > 0.2$). The 'wet' melts and high bulk silicate Moon estimated by Hui et al. were likely also overestimated because of the unrealistic assumption that the feldspars measured were the "first" to form from the lunar magma ocean.

There is no need to convert from H to H_2O, accounting for their different mass fractions, in order to directly compare the reported concentrations to other H_2O measurements that use the oxide convention, see revised Tables 2 and 3. Except for the potentially misleading axis labels in Figs. 15 and 16 (Simon et al., 2020) the findings and our interpretations of these data remain unchanged. The left panel of Fig. 1 modified after Fig. 15 of Simon et al. (2020) shown with the oxide nomenclature illustrates the inferred H_2O content in feldspar, based on secondary ion microprobe measurements of $^{16}OH^-$ in feldspar, plotted against the K_2O/CaO ratio of the samples. The diagram constructed in Fig. 2 modified after Fig. 16 of Simon et al. (2020) shown with the oxide nomenclature illustrates how computed Rayleigh fractionation model curves compare to the residual water inferred by feldspar measurements reported by Hui et al. (2013), Mosenfelder et al. (2017), and Simon et al. (2020) in terms mass fraction of H_2O.

Likewise, the interpretations and conclusions of the original contribution remain unchanged, including as follows: The Moon accreted dry or degassed early as demonstrated by the ubiquitous evidence of extremely low inferred water content in ancient lunar *igneous* materials. The extremely dry, granitic clast material in 14321,1062, given its relatively low amount of microstructural evidence for shock metamorphism, gives the best estimate for the inferred water content (~0.2 wt.% H_2O) of the felsic endmember of differentiation of the bulk Moon. The 'wet' felsic melts tentatively ascribed to felsite clast materials in Apollo samples 12,013 and 15,405 (i.e., Mills et al., 2017) are in assemblages that exhibit significant microstructural evidence of shock. They likely obtained little hydrogen from the lunar interior, but rather incorporated volatiles during an impact event involving a volatile-bearing impactor. It will be important to test the conclusions of this work by studying additional ancient felsic materials to evaluate further whether there is any lunar silicic magmatism that exhibits evidence for terrestrial abundances of magmatic water.

Declaration of Competing Interest

The authors declare that they have no known competing financial interests or personal relationships that could have appeared to influence the work reported in this paper.

References

Hamada M., Ushioda M., Fujii T. and Takahashi E. (2013) Hydrogen concentration in plagioclase as a hygrometer of arc basaltic melts: Approaches from melt inclusion analyses and hydrous melting experiments. *Earth Planet. Sci. Lett.* **365**, 253–262.

Haskin L. A., Shih C.-Y., Bansal B. M., Rhodes J. M., Wiesmann H. and Nyquist L. E. (1974) Chemical evidence for the origin of 76535 as a cumulate. *Lunar Planet. Sci. Conf. Proc.* **5**, 1213–1225.

Hui H., Guan Y., Chen Y., Peslier A. H., Zhang Y., Liu Y., Flemming R. L., Rossman G. R., Eiler J. M., Neal C. R. and Osinski G. R. (2017) A heterogeneous lunar interior for hydrogen isotopes as revealed by the lunar highland samples. *Earth Planet. Sci. Lett.* **473**, 14–23.

Hui H., Peslier A. H., Zhang Y. and Neal C. R. (2013) Water in lunar anorthosites and evidence for a wet early Moon. *Nature Geosci.* **6**, 177–180.

Johnson E. A. (2006) Water in nominally anhydrous crustal minerals: Speciation, concentration, and geologic significance. In *Water in Nominally Anhydrous Minerals* (eds. H. Keppler and J. R. Smyth). Geochemical Society/Mineralogical Society of America, Chantilly, VA, pp. 117–154.

Johnson E. A. and Rossman G. R. (2004) A survey of hydrous species and concentrations in igneous feldspar. *Am. Mineral.* **89**, 560–600.

Mills R. D., Simon J. I., Alexander C. M. O. D., Wang J. and Hauri E. H. (2017) Water in alkali feldspar: The effect of rhyolite generation on the lunar hydrogen budget. *Geochem. Perspect. Lett.* **3**, 115–123.

Mosenfelder J. L., Caseres J. R. and Hirschmann M. M. (2017) A comprehensive SIMS study of hydrogen, fluorine, and chlorine in nominally anhydrous minerals from 15 lunar samples. *48th Lunar and Planetary Science Conf. abstract #2473*.

Mosenfelder J. L., Rossman G. R. and Johnson E. A. (2015) Hydrous species in feldspars: A reassessment based on FTIR and SIMS. *Am. Min.* **100**, 1209–1221.

Mosenfelder, J.L. and Hirschmann, M.M. (2016) SIMS Measurements of Hydrogen and Fluorine in Lunar Nominally Anhydrous Minerals, 47th Lunar and Planetary Science Conference. LPI, The Woodlands, Texas, p. Abst. # 1903.

Quick J. E., Albee A. L., Ma M.-S., Murali A. V. and Schmitt R. A. (1977) Chemical compositions and possible immiscibility of two silicate melts in 12013. *Lunar Planet. Sci. Conf. Proc.* **8**, 2153–2189.

Ryder G. (1976) Lunar sample 15405 - Remnant of a KREEP basalt-granite differentiated pluton. *Earth Planet. Sci. Lett.* **29**, 255–268.

Simon J. I., Christoffersen R., Wang J., Mouser M. D., Mills R. D., Ross D. K., Rahman Z. and Alexander C. M. O'D. (2020) Volatiles in lunar felsite clasts: Impact-related delivery of hydrous material to an ancient dry lunar crust. *Geochim. Cosmochim. Acta* **276**, 299–326.

Schmitt A. K. and Simon J. I. (2004) Boron isotopic variations in hydrous rhyolitic melts: a case study from Long Valley. *California. Contrib. Miner. Petrol.* **146**, 590–605.

Wänke H., Palme H., Baddenhausen H., Dreibus G., Jagoutz E., Kruse H., Palme C., Spettel B., Teschke F. and Thacker R. (1975) New data on the chemistry of lunar samples – Primary matter in the lunar highlands and the bulk composition of the moon. *Lunar Planet. Sci. Conf. Proc.* **6**, 1313–1340.

Warren P. H., Taylor G. J., Keil K., Shirley D. N. and Wasson J. T. (1983) Petrology and chemistry of two "large" granite clasts from the Moon. *Earth Planet. Sci. Lett.* **64**, 175–185.

Warren P. H. and Wasson J. T. (1980) Further foraging for pristine nonmare rocks – Correlations between geochemistry and longitude. *Lunar Planet. Sci. Conf. Proc.* **11**, 431–470.